Journal of Geophysical Research: Oceans

RESEARCH ARTICLE
10.1029/2018JC014191

Energetics of the Southern Ocean Mode

A. Jüling[1], J. P. Viebahn[2], S. S. Drijfhout[1,3,4], and H. A. Dijkstra[1]

[1]Institute for Marine and Atmospheric research Utrecht, Department of Physics, Utrecht University, Utrecht, The Netherlands, [2]Centrum Wiskunde and Informatica, Amsterdam, The Netherlands, [3]National Oceanography Centre, Southampton, UK, [4]Royal Netherlands Meteorological Institute, De Bilt, The Netherlands

Abstract Recently, multidecadal variability in the Southern Ocean has been found in a strongly eddying global ocean circulation model. In this paper, we study the Lorenz energy cycle of this so-called Southern Ocean Mode (SOM). The Lorenz energy cycle analysis provides details on the energy pathways associated with the SOM. It shows that ocean eddies and the baroclinic energy pathway together with variations in the kinetic energy input by the wind are crucial aspects of the variability. It is also shown how convective mixing, which is induced by the SOM in particular in the Weddell Gyre, is responsible for the large-scale multidecadal variability in Antarctic Bottom Water and Atlantic Meridional Overturning Circulation.

Plain Language Summary Recently, large fluctuations of the oceanic heat content were discovered in the Atlantic sector of the Southern Ocean in an ocean simulation. These changes are periodic and repeat every 50 years, which is why we cannot confirm them from out limited observational record. We investigate this phenomenon through a mechanical energy perspective and find that it is likely caused by an interplay between eddies (the oceanic equivalent of atmospheric storms with 10- to 100-km diameter) and the average flow around Antarctica. In addition, we find connected sinking events that influence the ocean's overturning strength. If this phenomenon is found in the real ocean, it may influence the global mean surface temperature significantly over decades.

Key Points:
- The multidecadal varying Lorenz energy cycle of a global ocean model is analyzed
- A mechanical energy description of the Southern Ocean Mode is provided
- A detailed physical mechanism for the Southern Ocean Mode is proposed

Supporting Information:
- Figure S1
- Figure S2
- Figure S3
- Figure S4

Correspondence to:
A. Jüling,
a.juling@uu.nl

Citation:
Jüling, A., Viebahn, J. P., Drijfhout, S. S., & Dijkstra, H. A. (2018). Energetics of the Southern Ocean Mode. *Journal of Geophysical Research: Oceans*, *123*, 9283–9304. https://doi.org/10.1029/2018JC014191

Received 20 MAY 2018
Accepted 30 OCT 2018
Accepted article online 27 NOV 2018
Published online 26 DEC 2018

1. Introduction

The Southern Ocean is an important component in the climate system, as it is the world's most biologically productive ocean and a significant sink for both heat and CO_2 (Mayewski et al., 2009). The strong westerly winds over this region drive the Antarctic Circumpolar Current (ACC) and are also involved in driving the Atlantic meridional overturning circulation (AMOC). In fact, the coldest and densest water mass, the Antarctic Bottom Water (AABW), is produced here (Gordon, 1982).

Although the instrumental record is relatively sparse on Southern Ocean properties, sea surface temperature (SST) records indicate low-frequency variations, that is, on decadal-to-centennial timescales. For example, the Southern Ocean Centennial Variability index, which is the zonally and 50–70° S averaged SST anomaly (Latif et al., 2013), shows a minimum around 1930 and maxima near 1880 and 1975. During the second maximum of the Southern Ocean Centennial Variability, also, the Weddell Polynya, a large area free of sea ice, appeared (Gordon, 1978). This polynya did not appear again until very recently, indicating also the presence of variability on decadal-to-multidecadal timescales (Latif et al., 2017).

Many modeling studies have been carried out to understand what causes this low-frequency variability in the Southern Ocean. Pronounced centennial variability was found in a 1,500-year-long simulation with the Kiel Climate Model using present-day mean forcing conditions (Latif et al., 2013; Park & Latif, 2008). Analysis revealed that convection in the Weddell Sea is crucial for this variability with responses on sea ice extent and AMOC in turn affecting the heat transport in the Southern Ocean (Martin et al., 2013). Such low-frequency variability was also found in long control simulations of the GFDL CM2.1 model (Delworth & Zeng, 2012) and the HadCM3 model (Jackson & Vellinga, 2013).

In all of these model studies, the horizontal resolution of the ocean component is not sufficient to represent ocean eddies. It is known, however, that eddies have a major effect on the momentum and heat transport in the Southern Ocean (Gent, 2016). Dufour et al. (2017) showed that in a strongly eddying ocean model configuration periodic convection can occur, whereas quasi-continuous convection was found in a coarse resolution

configuration (0.1° vs. 0.25° grid spacing), due to the mesoscale eddies' restratifying effects. It is expected then that also the low-frequency variability in ocean models is affected by their capability of representing eddies. To study this problem, long interval simulations with high-resolution models are necessary. Such simulations have now been performed (Maltrud et al., 2010) and have proven to realistically produce many features of the oceanic general circulation.

Recently, output from a 326-year simulation with a strongly eddying (a horizontal grid spacing of 0.1°) version of the Parallel Ocean Program (POP) revealed multidecadal (40- to 50-year) spatiotemporal variability in the Southern Ocean (Le Bars et al., 2016), termed the Southern Ocean Mode (SOM). Although the spatial pattern of the SST anomalies spans the full Southern Ocean, large-scale anomalies occur in the Weddell Sea area. The SOM cannot be validated from the instrumental record, but if it exists, it should have many teleconnections to variability elsewhere. As such, the SOM has recently been suggested to influence variability of the North Brazil Current through the propagation of Rossby waves (van Westen & Dijkstra, 2017).

A first description of the mechanisms of the SOM was presented in Le Bars et al. (2016). It was shown that the changes in overall potential energy (PE) and kinetic energy (KE) in the region south of 30° S (associated with the SOM) could be linked to a dynamical mechanism described by Hogg and Blundell (2006) who used an idealized quasi-geostrophic model. In particular, eddies are thought to be crucial for the existence of the SOM, because the SOM does not appear in a global 1° horizontal grid spacing version of POP. However, the role of the eddies was not made explicit in the analysis of Le Bars et al. (2016). On the other hand, it was shown that the peak-to-peak anomaly in global ocean heat content associated with the SOM is about 60 ZJ, which may make it a highly relevant for climate variability. It is therefore important to understand the physical mechanism of the SOM in more detail than presented in Le Bars et al. (2016).

A next step to analyze the multidecadal SOM variability is to investigate the eddy-mean decomposed Lorenz energy cycle (LEC). For the atmosphere, the LEC has been proven to be a useful concept for analyzing dynamical processes (Lorenz, 1955). It is well accepted that the atmosphere works as a heat engine that operates between warm sources at low latitudes near the surface and cold sinks at high latitudes in the upper atmosphere, thereby converting thermal energy into mechanical energy in order to maintain the KE of the circulations against a continuous drain of energy by frictional dissipation (Oort & Peixóto, 1983). However, the detailed quantitative description of the oceanic energy cycle is still in the beginning, and many uncertainties remain (Ferrari & Wunsch, 2009), the main difficulty being the limited temporal and spatial coverage of oceanic observations.

Recently, an LEC analysis has been performed on global strongly eddying ocean models (von Storch et al., 2012; Wu et al., 2017), where only the time-mean energy compartment content and conversions were considered. In the Max Planck Institute ocean model (with 0.1° horizontal grid spacing), von Storch et al. (2012) show that globally about 6.6 TW of energy is generated, of which 4.1 TW by the wind stress. The largest energy conversion mechanism (about 0.75 TW) is the baroclinic pathway, which is facilitated both by the buoyancy flux and the wind stress, the latter through upwelling. Wu et al. (2017) use the LEC analysis to understand the response of their model (the MITgcm at about 0.2° horizontal grid spacing) to changes in the surface winds stress. The latter problem is also studied in Hogg et al. (2017) using results from a GFDL CM2.5 model (horizontal grid spacing about 0.25°) simulation (Griffies et al., 2015). An overall energy analysis, where the reference minimum PE state is determined from the density field, was performed.

In addition to periodic changes in the energy components of the LEC, open ocean convection in the Weddell Gyre is seen in the POP simulation cooscillating with the SOM. Open ocean convection is a feature of many CMIP5 models (Heuzé et al., 2013); however, the regularity suggests a link to the SOM mechanism. This is particularly interesting in light of the recently observed Weddell Polynya in 2016–2017, which returned some four decades after it was first observed in 1973–1974 (Scambos et al., 2018).

This paper is focussed on understanding the multidecadal variability in the Southern Ocean associated with the SOM and extends previous LEC studies precisely in the aspect of low-frequency variability. Section 2 provides a brief description of the model setup and the POP simulation that displays the SOM. It further details the multidecadal variability found in the strongly eddying POP simulation. Section 3 presents the formulation of the LEC and discusses convection in the LEC framework. Section 4 characterizes the temporal and spatial variability of the four major energy reservoirs, their associated generation terms, and the energy exchanges

between the reservoirs. A description of the mechanism of the SOM is provided in section 5, and the paper concludes with a summary and discussion in section 6.

2. Intrinsic Multidecadal Ocean Variability

In this study, we continue the investigation of output of a strongly eddying global ocean model simulation, previously presented in Weijer et al. (2012) and Le Bars et al. (2016).

2.1. Model Simulation

The global ocean simulation is performed using the POP (Dukowicz & Smith, 1994), developed at Los Alamos National Laboratory. The strongly eddying configuration of POP is based on that used by Maltrud et al. (2010), with an average 0.1° horizontal grid spacing and 42 vertical levels. The atmospheric forcing of the model is based on the repeat annual cycle (normal year) Coordinated Ocean Reference Experiment (see http://www.clivar.org/organization/wgomd/core) forcing data set (Large & Yeager, 2004), with 6-hourly forcing averaged to monthly. Wind stress is computed offline using the Hurrell SST climatology (Hurrell et al., 2008) and standard bulk formulae. Evaporation and sensible heat flux were calculated online using bulk formulae and the model-calculated SST. Precipitation was also taken from the Coordinated Ocean Reference Experiment forcing data set. Sea ice cover was prescribed based on the −1.8°C isotherm of the SST climatology (the sea ice fraction increases linearly to 100% between −0.8°C and −1.8°C), with both temperature and salinity restored on a timescale of 30 days under diagnosed climatological sea ice. The salinity restoration is intended to mimic sea ice processes such as brine rejection and melt. While the momentum transfer is not affected by the presence of sea ice, the heat flux (calculated assuming no sea ice) is multiplied by a factor of 1 (sea ice fraction).

The initial conditions are the final state of a 75-year spin-up simulation described in Maltrud et al. (2010) with restoring conditions for salinity. The freshwater flux was diagnosed during the last 5 years of this spin-up simulation, and the simulation presented in Le Bars et al. (2016) applies this diagnosed freshwater flux, and no restoring of salinity is used. The model configuration and simulation procedure is discussed in detail in the supplementary material of Weijer et al. (2012). The POP simulation analyzed in Le Bars et al. (2016) used 251 years of data. Over the last 51 years of this simulation (model years 276–326) the terms of the mechanical energy budget for primitive equations (following von Storch et al., 2012; see below) are written out and used for analysis.

2.2. The Southern Ocean Mode

As presented in Le Bars et al. (2016), the 0.1° POP simulation exhibits a mode of intrinsic multidecadal variability, the so-called the SOM, which is localized in the Southern Ocean, between the South Atlantic and the Weddell Gyre. This spatiotemporal variability has a period of 40–50 years, and the peak-to-peak difference in global ocean heat content within a multidecadal cycle is up to 60 ZJ. This change results from surface heat flux variations in the Atlantic sector of the Southern Ocean and propagation of temperature anomalies along the ACC and into the Weddell Gyre around 30°E. The temperature anomalies propagate as deep as 5,000 m along isopycnals between 50°S and 30°S.

The SOM index was calculated as in Le Bars et al. (2016), as the SST anomaly over the region (0–50° W × 35–50° S) and is shown as the blue curve in Figures 1a and 1b. The multidecadal variations associated with the SOM are directly visible in a broad range of ocean fields. Figure 1a also shows time series of the Drake Passage volume transport (orange) and the maximum Weddell Gyre volume transport (red). The two transports are anticorrelated and both show multidecadal variations of about 10 Sv. Figure 1b shows time series of the southward North Atlantic Deep Water (NADW) volume transport (purple) and the northward AABW volume transport (green) at 30°S. Also, these two signals display very regular multidecadal variations of about 2 Sv, which are essentially anticorrelated.

Moreover, open ocean deep convection events in the Weddell Gyre region are associated with the SOM. The deep convection can be recognized in the model mixed layer depth (MLD). The MLD is defined as the shallowest depth where the local, interpolated buoyancy gradient matches the maximum buoyancy gradient between the surface and any discrete depth within that water column (Smith et al., 2010). As such it can be interpreted as the deepest penetration of turbulent mixing. The MLD time series of Figure 1 shows the yearly maximum MLD in the Weddell Gyre to Kerguelen Plateau (WGKP) region with maxima occurring during austral winter when cooling, and hence, thermal buoyancy forcing is strongest. Figure 2a shows the time-mean

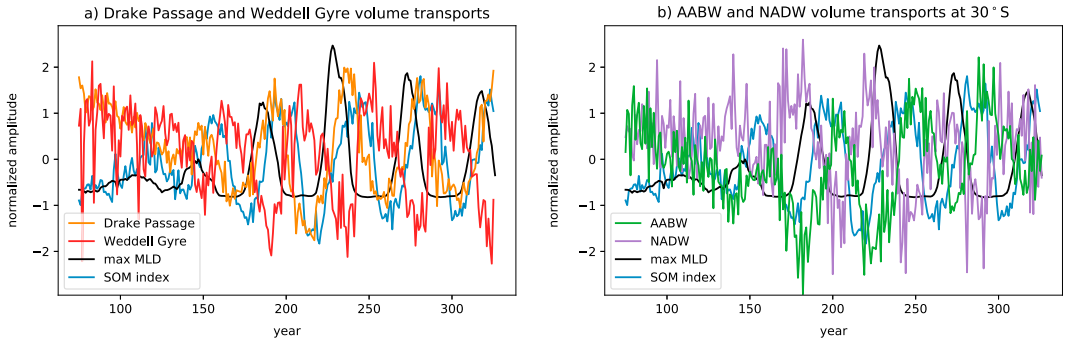

Figure 1. (a) Drake Passage (orange) and Weddell Gyre (red) normalized volume transports. The respective means and standard deviations of the years 200–326 are 109 ± 5.2 Sv and 81.8 ± 5.4 Sv. (b) Southward NADW transport (purple) and northward AABW (green) transport at 30°S. The respective means and standard deviations of the years 200–326 are 12.3 ± 2 Sv and 11.0 ± 2 Sv. For comparison the maximum MLD in the Weddell Gyre region (black) and the SOM index (blue) are shown in both (a) and (b). AABW = Antarctic Bottom Water; MLD = mixed layer depth; NADW = North Atlantic Deep Water; SOM = Southern Ocean Mode.

maximum MLD in the Weddell Gyre region, and Figure 2b shows the time series of yearly maximum MLD on top of potential temperature anomalies. The POP simulation generates maximum MLDs of up to 4,000-m deep in the Weddell Sea region.

The sinking of dense water in the open ocean to the deep ocean drives a stronger abyssal circulation. Consequently, the northward AABW volume transport (green, Figure 1b) increases in response to the deep convection. Note that the response of the northward AABW volume transport shows a significant lag in our time series. The delay of the Drake Passage transport increase (orange, Figure 1a) is shorter because it is a more direct geostrophic response to an increased north-south density gradient, while for the deep AABW overturning cell a geostrophic response is only possible after the density anomaly created by convection is transported from its origin to the eastern boundary of the South Atlantic. The resulting change in east-west density difference also affects the east-west pressure gradient of the overlying AMOC in such a way that the AMOC anticorrelates with the deeper AABW cell. For this reason the AMOC shows a lagged anticorrelation

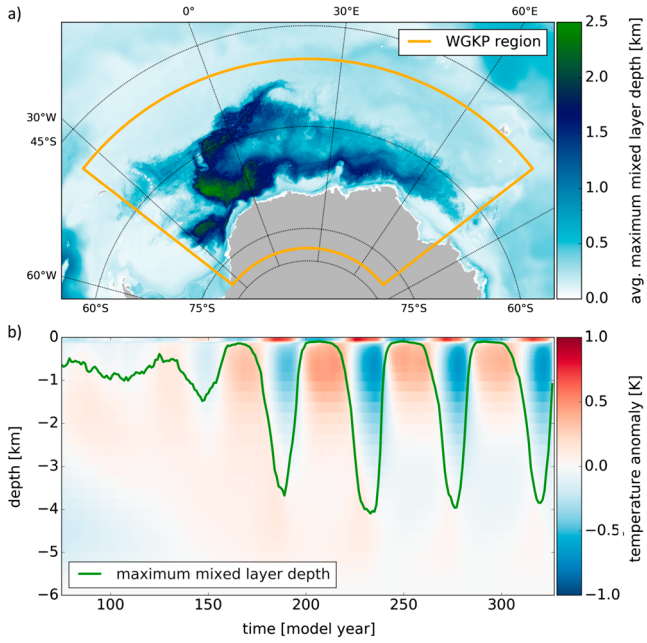

Figure 2. (a) Time-mean maximum mixed layer depth in the Weddell Gyre region. The yellow lines enclose the so-called "Weddell Gyre to Kerguelen Plateau" (WGKP) region, defined by [90°S, 50°S] × [35°W, 80°E]. (b) Time series of maximum mixed layer depth on top of potential temperature anomalies. Heat builds up at depth and is released during convective events, cooling the deep waters and heating the surface waters.

with Drake Passage transport and the AABW a lagged-correlation with Drake Passage transport. Furthermore, the enhanced lower branch of the AMOC is directly linked to the stronger zonal transport (orange, Figure 1a), as also found in previous studies (Behrens et al., 2016; Gent et al., 2001; Howard et al., 2015).

3. Lorenz Energy Cycle

Although the details of the LEC are presented extensively in von Storch et al. (2012) and Wu et al. (2017), we provide a short summary for self-consistency and for helping a less specialist reader to interpret the results in the sections 4 and 5. The LEC deals with the evolution of terms in the mechanical energy balance, involving kinetic and available potential energy (APE). The APE of a state of the system is the difference between the PE of this state and an adiabatically redistributed, minimal PE background state of the same water masses. Calculating this ground state is not trivial in the case of complex bathymetry as basins can be isolated from one another (Hogg et al., 2017).

3.1. Formulation

As a reference state for the calculation of the APE, we follow von Storch et al. (2012) to use the global (area) average of the potential density ρ in each model layer, that is,

$$\rho_{ref}(z) = \langle \rho(x, y, z, t) \rangle_{av}, \tag{1}$$

where the angled brackets indicate an area average while the average subscript denotes the time average of 51 years (i.e., over an entire cycle of the SOM). The resulting density profile $\rho_{ref}(z)$ is stably stratified, and density anomalies are defined as the departure from this reference density, that is,

$$\rho^*(x, y, z, t) = \rho(x, y, z, t) - \rho_{ref}(z). \tag{2}$$

In the following we use a time average of 5 years (i.e., *not* over an entire cycle of the SOM) in order to perform the eddy-mean decomposition, and this time average is indicated by a bar. Anomalies with respect to this time average are indicated by a prime. In this way the LEC terms become temporally dependent. KE and APE reservoirs are symbolized by K and P . The energy content of the mean and eddy APE reservoirs is calculated from

$$P_m = -\frac{g}{2} \int_V \frac{1}{n_0} \bar{\rho}^{*2} \, \mathrm{d}V, \tag{3a}$$

$$P_e = -\frac{g}{2} \int_V \frac{1}{n_0} \overline{\rho^{*\prime 2}} \mathrm{d}V, \tag{3b}$$

where $g = 9.81$ m/s^2 is the gravitational acceleration, $n_0(z)$ is the vertical gradient of the reference potential density, and V denotes the volume over which the LEC is considered. The density terms can be rewritten in the following way:

$$\bar{\rho}^{*2} = \left(\bar{\rho} - \rho_{ref}\right)^2, \tag{4a}$$

$$\overline{\rho^{*\prime 2}} = \overline{\left(\rho - \rho_{ref}\right)^{\prime 2}} = \overline{\left(\rho - \rho_{ref}\right)^2} - \overline{\left(\rho - \rho_{ref}\right)}^2 = \overline{\rho^2} - \bar{\rho}^2. \tag{4b}$$

The absolute content of the P reservoirs is not relevant because of the arbitrary reference level.

The energy content of the KE reservoirs can be computed as

$$K_m = \frac{\rho_0}{2} \int_V \left(\bar{u}^2 + \bar{v}^2\right) \, \mathrm{d}V, \tag{5a}$$

$$K_e = \frac{\rho_0}{2} \int_V \left(\overline{u^{\prime 2} + v^{\prime 2}}\right) \, \mathrm{d}V, \tag{5b}$$

where $\mathbf{u} = (u, v)$ indicates the horizontal velocity vector. For example, the zonal component of the K_e-term is $\overline{u^{\prime 2}} = \overline{u^2} - \bar{u}^2$ as per Eulerian mean decomposition. The density $\rho_0 = 1{,}026$ kg/m^3 is the global average density of sea water.

The evolution of the energy content of the different reservoirs can now be written as (von Storch et al., 2012)

$$\frac{dK_m}{dt} = G(K_m) + C(K_e, K_m) + C(P_m, K_m) + B(K_m) - D(K_m), \tag{6a}$$

$$\frac{dK_e}{dt} = G(K_e) - C(K_e, K_m) + C(P_e, K_e) + B(K_e) - D(K_e), \tag{6b}$$

$$\frac{dP_m}{dt} = G(P_m) + C(P_e, P_m) - C(P_m, K_m) + B(P_m) - D(P_m), \tag{6c}$$

$$\frac{dP_e}{dt} = G(P_e) - C(P_e, P_m) - C(P_e, K_e) + B(P_e) - D(P_e), \tag{6d}$$

where the generation of X is denoted by $G(X)$, conversion from X to Y by $C(X, Y)$ (and hence, $C(Y, X) = -C(X, Y)$) and dissipation of X by $D(X)$. Boundary terms arise when a regional domain is chosen and are indicated by the terms $B(X)$, which are positive when property X enters the volume through the boundary.

For the interpretation of the results below, the generation and conversion terms are most important. Kinetic energy is generated by the wind exerting a stress on the ocean surface S transferring momentum to the water. The terms $G(K_m)$ and $G(K_e)$ represent this energy input and are given by

$$G(K_m) = \int_S \left(\overline{\tau_x}\bar{u} + \overline{\tau_y}\bar{v}\right) \mathrm{d}S, \tag{7a}$$

$$G(K_e) = \int_S \left(\overline{\tau_x' u'} + \overline{\tau_y' v'}\right) \mathrm{d}S, \tag{7b}$$

with $\tau = (\tau_x, \tau_y)$ being the wind stress.

The generation of APE occurs due to buoyancy fluxes at the surface of the ocean, and the terms $G(P_m)$ and $G(P_e)$ are given by

$$G(P_m) = -g \int_S \left(\underbrace{\frac{\alpha_{0,1}}{n_0} \overline{J_s \rho^*}}_{\text{heat}} + \underbrace{\frac{\beta_{0,1}}{n_0} \overline{G_s \rho^*}}_{\text{salt}} \right) \mathrm{d}S, \tag{8a}$$

$$G(P_e) = -g \int_S \left(\underbrace{\frac{\alpha_{0,1}}{n_0} \overline{J_s' \rho'}}_{\text{heat}} + \underbrace{\frac{\beta_{0,1}}{n_0} \overline{G_s' \rho'}}_{\text{salt}} \right) \mathrm{d}S, \tag{8b}$$

where $\alpha_{0,1}$ and $\beta_{0,1}$ are the temperature and salinity expansion coefficients in the equation of state in the uppermost model layer, respectively. Furthermore, $J_s = H/(\rho_0 c)$ and $G_s = \bar{S}_0(E - P)$, where H is the total heat flux, c = 3,996 J·kg^{-1}·K^{-1} the specific heat of sea water, $\bar{S}_0$ the time-mean surface salinity, and $(E - P)$ the difference between evaporation and precipitation.

The first conversion term is that of eddy to mean KE $C(K_e, K_m)$, given by

$$C(K_e, K_m) = \rho_0 \int_V \left(\overline{u'\mathbf{u}'} \cdot \nabla \bar{u} + \overline{v'\mathbf{u}'} \cdot \nabla \bar{v} \right) \mathrm{d}V, \tag{9}$$

and represents the energy pathway from mean to eddies through the Reynolds' stress (e.g., due to barotropic instability, where $C(K_e, K_m) < 0$). Von Storch et al. (2012) showed that globally, $C(K_e, K_m) = -0.11$ TW, indicating the relevance of the barotropic instability process to the global LEC.

The second term is the conversion between mean and eddy PE, given by

$$C(P_e, P_m) = -\int_V \frac{g}{n_0} \overline{\rho' \mathbf{u}_h'} \cdot \nabla_h \bar{\rho} \, \mathrm{d}V, \tag{10}$$

where the subscript h indicates the horizontal components. The sign and magnitude of this term depend on the orientation of the eddy density flux $\overline{\rho' \mathbf{u}_h'}$ and the mean horizontal density gradient $\nabla_h \bar{\rho}$. Transfer of energy from mean to eddy PE (hence with $C(P_e, P_m) < 0$) occurs due to baroclinic instability, which requires sloped isopycnals. Von Storch et al. (2012) showed that globally, $C(P_e, P_m) = -0.83$ TW, indicating the importance of the baroclinic instability process to the global LEC.

PE can be converted into KE via vertical advection of potential density. The term $C(P_m, K_m)$, given by

$$C(P_m, K_m) = -g \int_V \bar{\rho}\bar{w}\, dV, \tag{11}$$

gives only a contribution when the density of the water that is transported upward differs from the density of the water that is transported downward. Hence, upwelling of cold water (e.g., by Ekman pumping) increases the mean PE, and hence, $C(P_m, K_m) < 0$. Von Storch et al. (2012) showed that globally, $C(P_m, K_m) = -0.5$ TW, indicating the importance of this conversion process to the global LEC.

Similarly, the presence of eddies can change the eddy PE reservoir P_e, through the term $C(P_e, K_e)$, defined by

$$C(P_e, K_e) = -g \int_V \overline{\rho' w'}\, dV, \tag{12}$$

if there is a net correlation between the vertical velocity field and the density anomalies (i.e., a net upwelling of colder water would give $C(P_e, K_e) < 0$). Such a correlation exists in the baroclinic instability process, where isopycnal slopes are reduced, and hence, $C(P_e, K_e) > 0$ (+0.74 TW globally in von Storch et al., 2012).

The dissipation terms $D(X)$ are calculated, assuming constant reservoir sizes as in von Storch et al. (2012). This simplification is justified, as the change in reservoir sizes is much smaller than the fluxes affecting them. For nonglobal integrals, boundary terms appear. Except for the K_m boundary terms, these are not explicitly calculated but rather combined with the dissipation terms. Between the K_m boundary terms of advection by mean and eddy fluxes and viscous effects, the pressure work term is dominant and henceforth the one we present as the boundary term

$$B(K_m) = \int_V \nabla_h \cdot \mathbf{u}_h p^*\, dV, \tag{13}$$

where p^* is the hydrostatic pressure anomaly with respect to the time- and area-mean hydrostatic reference pressure profile $p_{ref}(z) = \langle p(x, y, z, t) \rangle_{av}$, akin to the reference profile $\rho_{ref}(z)$ (equation (1)).

3.2. Convection in the LEC

As convective processes are discussed later, this is a good moment to mention how these processes are represented in the LEC. In ocean models like POP, vertical mixing of heat and salt will occur when the stratification becomes unstable. In POP this is implemented through the KPP scheme where a deepening of the mixed layer occurs due to the vertical mixing of the properties determining the density (i.e., temperature T and salinity S). However, there are no vertical velocities associated with this vertical mixing due to the hydrostatic approximation in POP, and hence, these processes are not represented explicitly in the LEC analysis. They can be considered ad hoc, such as in the ocean model used in Dijkstra et al. (2014) and in the analysis of Hogg et al. (2017), but such an approach is still not energetically consistent (see both references for a more extensive discussion). There is another caveat to interpret the effect of convective processes in a LEC analysis, as it is assumed that the vertical density gradient does not deviate strongly from the area (global) mean profile (connected to $n_0(z)$ in the analysis above), whereas during convection isopycnals will become nearly vertical.

However, the vertical mixing of density will have an effect on the horizontal density gradients as this mixing will be horizontally inhomogeneous. Hence, the effects of convection will at least show up in the terms $C(P_m, P_e)$ (which is affected by the horizontal density gradients) and in the term $C(P_m, K_m)$, the latter through the mean density structure $\bar{\rho}$. For example, if convective mixing increases the density at depth, then, in the presence of background upwelling, the term $C(P_m, K_m) < 0$, and the energy content of reservoir P_m increases. Simultaneously, the large horizontal density gradients that are created will also lead to a higher dissipation of APE (which is proportional to $\nabla^2\rho$), and hence, the increased conversion to P_m due to the vertical mixing may be partially balanced by a higher dissipation and may not be completely available for the baroclinic pathway. As will be discussed later, the response of these conversions terms to changes in deep convection cannot be understood by the act of convection alone but must also include how the (overturning) circulation responds to changes in deep convection.

4. An LEC Description of the SOM

First the mean and standard deviation of the LEC components are presented in section 4.1. In section 4.2, the multidecadal changes in the spatial fields of specific LEC components are discussed, and finally (section 4.3), the temporal changes of spatially averaged fields are described.

4.1. Temporal Mean and Standard Deviation of Spatially Integrated LEC Terms

In this section we present the temporal average (over the entire cycle of the SOM) of the spatially integrated LEC terms. The corresponding block diagrams in Figure 3 can be directly compared with the previous studies by von Storch et al. (2012; global integrals, their Figure 13) and Wu et al. (2017; SO integrals, their Figure 15).

Figure 3a shows the temporal mean and standard deviation of the globally integrated LEC. For this case, the boundary terms B are zero, and the dissipation terms D are calculated from Figure (6d) assuming steady balances. The time-mean values are very similar to the values found by von Storch et al. (2012; see their Figure 13a). Regarding the energy reservoirs, the mean APE P_m is much larger than the other three reservoirs. The exact value of P_m is, however, not particularly meaningful due to its dependence on the choice of the reference density. The other three reservoirs share the same order of magnitude as P_e with $P_e > K_e > K_m$.

The conversion terms exhibit the pronounced baroclinic pathway $P_m \rightarrow P_e \rightarrow K_e$, characterized by a conversion from the mean APE to the eddy APE ($C(P_m, P_e)$) that has about the same magnitude (power of about 1 TW) as the conversion from the eddy PE to the eddy KE ($C(P_e, K_e)$). Oceanic mesoscale eddies are, to a large extent, generated by baroclinic instability via the baroclinic route $P_m \rightarrow P_e \rightarrow K_e$. Moreover, the negative sign of $C(P_m, K_m)$ indicates that the oceanic time-mean circulation, being fueled by the winds, converts its KE into the mean APE by Ekman pumping. This conversion substantially facilitates density differences and hence the mean APE from which the baroclinic pathway originates. Finally, the oceanic mean circulation converts its KE also into the eddy KE as can be seen from the negative sign of $C(K_e, K_m)$.

The generation rates $G(P_m)$ and $G(K_m)$ as well as the dissipation rates $D(P_m)$ and $D(K_m)$ are much larger than the related conversion rates. Thus, to a first approximation, $G(P_m)$ and $G(K_m)$ are balanced by $D(P_m)$ and $D(K_m)$, respectively, indicating that the conversion rates are of second-order importance in determining the reservoirs P_m and K_m. The latter are essential to connect the LEC framework with the SOM. In contrast, the generation rates $G(P_e)$ and $G(K_e)$ are significantly smaller, which is, however, partly due to the slowly varying forcing fields employed in our simulation (i.e., monthly variations in contrast to, e.g., 6-hourly variations used in von Storch et al. (2012). Nevertheless, $D(K_e)$ has a magnitude that is similar to the magnitudes of $D(P_m)$ and $D(K_m)$, which is due to the directions of the two energy pathways $K_m \rightarrow P_m \rightarrow P_e \rightarrow K_e$ and $K_m \rightarrow K_e$.

Figure 3b shows the temporal mean and standard deviation of the LEC integrated within the Southern Ocean (SO30, i.e., the region south of 30°S), which can be compared with the results given by Wu et al. (2017; see their Figure 15). Here only one boundary term $B(K_m)$ is explicitly computed (see Figure S1 in the supporting information), and for all the other quantities, the $B-D$ term (indicated by D/B in Figure 3b) is calculated again from Figure (6d) assuming steady balances. The LEC within the SO shares many properties with the global LEC: Regarding the reservoirs it also holds $P_m \gg P_e > K_e > K_m$ (also found by Wu et al., 2017) with about 50% of the global K_m and K_e being located in the SO in our model simulation. Also, within the SO the energy pathways are given by $K_m \rightarrow P_m \rightarrow P_e \rightarrow K_e$ and $K_m \rightarrow K_e$ (also found by Wu et al., 2017). The conversion term $C(K_m, P_m)$ is especially large (accounting for about 0% of the global value) and related to the Ekman pumping (Deacon cell) in the SO, which is particularly strong in our POP simulation. About 50% of the conversions $C(K_m, K_e)$ and $C(P_e, K_e)$ are located in the SO such that $C(P_e, K_e) > C(K_m, K_e)$ also holds within the SO.

The crucial role of the winds as main energy supplier for the ocean is extreme within the SO in our simulation (but generally also found by Wu et al., 2017). In the SO, the generation rate $G(K_m)$ accounts for about 56% of the corresponding global value and, most strikingly, for about 95% of the total energy input within the SO (Wu et al., 2017, report values of 71%). This is related, on the one hand, to the slowly varying forcing fields employed in our simulation (such that $G(K_e)$ and $G(P_e)$ are relatively small) and, on the other hand, to the fact that the thermal and saline buoyancy forcing contributions largely compensate each other within the SO in our simulation (such that the $G(P)$ terms are relatively small). Our value of $G(K_m)$ in the SO is about twice as large as the corresponding value in Wu et al. (2017), and, consequently, our values of the energy reservoirs in the SO are also significantly larger than in Wu et al. (2017; they find that all the energy reservoirs increase under stronger wind forcing). The total generation of KE of 1.34 TW is, however, comparable to those of Wu et al. (2017; 1.17 TW and 1.46 TW in their two scenarios). Similarly, von Storch et al. (2012) globally find an approximate equipartition between the mean and eddy KE generation terms, while we find—again due to the monthly versus 6-hourly forcing—a significantly larger contribution in the mean component. One consequence of a stronger $G(K_m)$ input is that the energy flows away from the K_m reservoir, namely, $D(K_m)$, $-C(P_m, K_m)$, $C(K_m, K_e)$, and $B(K_m)$, are stronger than in the study of Wu et al. (2017).

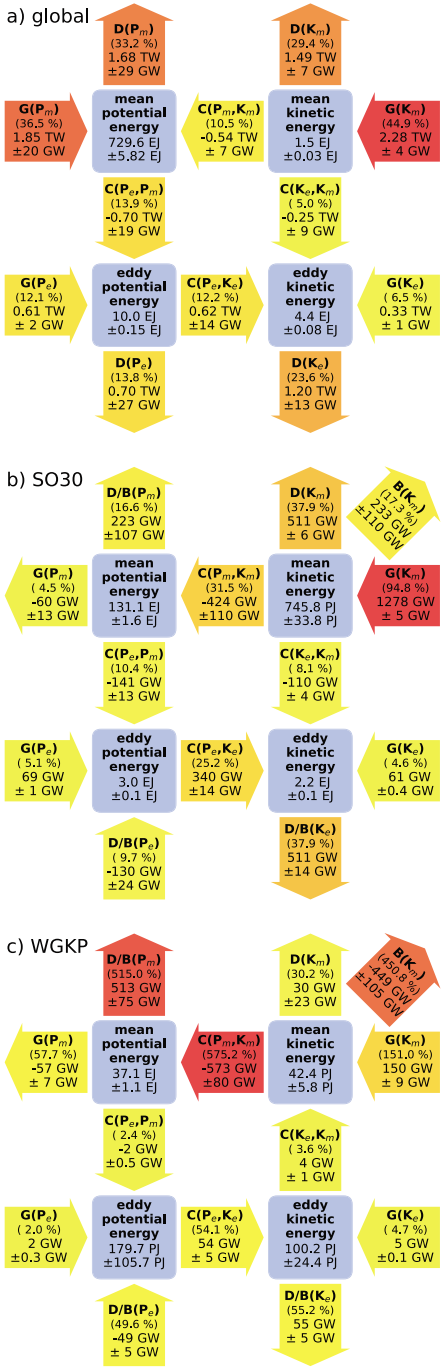

Figure 3. Lorenz energy cycle terms that are temporally averaged over one cycle of the Southern Ocean Mode and spatially integrated over the globe (a), the Southern Ocean region up to 30°S (SO30; b), and the Weddell Gyre to Kerguelen Plateau region (WGKP; c). The blue rounded squares represent the energy reservoirs, while the arrows represent energy transfer terms: G = generation, C = conversion, and D = dissipation. The percentages in parentheses are the ratio of the term to the total generation (which is also reflected in the colors: red, strongest, to yellow, weakest). Shown are the mean values, and the ± values are the standard deviations.

The variances of the different LEC terms in the SO are very similar to the variances of the corresponding global LEC terms, and generally slightly larger than the variances given by Wu et al. (2017). The one outstanding exception is the conversion term $C(K_m, P_m)$ integrated within the SO that exhibits a drastically larger variance than the variance of the corresponding global integral as well as to the value found by Wu et al. (2017) for the SO. Since all other conversion, generation, and reservoir terms in the SO exhibit much smaller variances, the variability in $C(K_m, P_m)$ within the SO must be balanced either by dissipation within the SO or by the northern boundary exchange term (i.e., outside of the SO).

For the K_m-budget we find that the northern boundary exchange term $B(K_m)$ is crucial. More precisely, in the time mean $B(K_m)$ exports about half as much K_m out of the SO as $C(K_m, P_m)$ (also found by Wu et al., 2017). More importantly, $B(K_m)$ exhibits the same variance as $C(K_m, P_m)$ (in contrast to Wu et al., 2017) and hence is balancing the variability of $C(K_m, P_m)$ in the K_m budget in our simulation (see also section 4.3). Consequently, in the presence of the intrinsic multidecadal variability exhibited by our model simulation, the northern boundary exchange terms are relevant in order to close the K_m and P_m budgets. This stands in contrast to the results of Wu et al. (2017), who find that the energy flows at the northern boundary are significantly weaker than the energy conversion rates inside the SO (especially the variances).

Finally, we also consider the LEC terms integrated within the much smaller WGKP region (defined in Figure 2a), and results are shown in Figure 3c. The mean values of all reservoirs decrease by about 1 order of magnitude (with respect to the SO30 results) such that it still holds $P_m \gg P_e > K_e > K_m$. However, in contrast to the SO30 results, the mean energetics and the eddy energetics appear to be largely decoupled in the WGKP region since two conversions $C(P_m, P_e)$ and $C(K_m, K_e)$ are drastically smaller both in mean value as in variance. The conversion $C(K_m, P_m)$ and the generation rate $G(P_m)$, on the other hand, depict mean and variance values similar to the SO30 results, indicating that most of the SOM variability is located in the WGKP region. This also suggests that convection rather than baroclinic instability is the dominant process in the WGKP region and hence an integral part of the intrinsic multidecadal variability of the mean energy reservoirs. The eddy reservoirs in the WGKP region, on the other hand, appear to be largely driven by the import of P_e via the boundaries, which in turn is transferred to K_e via $C(P_e, K_e)$ and then dissipated.

4.2. Spatial Distributions of the LEC Terms

Having discussed the temporal mean and standard deviation of the spatially integrated LEC terms, in this section, we look at the local (i.e., spatially distributed) LEC terms in the SO averaged over four phases.

We adopt the phase choice by Le Bars et al. (2016) who based it on the variability of the total potential and kinetic energies because these phases coincide very well with the variability of the deep convection in the Weddell Gyre (see, e.g., Figure 10). The reference phase (*D*) during years 286–300 exhibits no convection, while the phase of strong convection (*B*) comprises the years 311–320, and the transition phases *A* and *C* consist of years 301–310 and 278–285, 321–326, respectively. We note that by defining the reference state by phase *D* the anomaly patterns are largely spatially stationary for LEC fields depicting anomalies with large-scale spatial structures (e.g., P_m and P_e in Figure 4, $G(P_m)$ in Figures 6a–6d, and K_e in Figures 5e–5h). In contrast, if the reference mean is, for example, defined over the entire SOM cycle, then the anomaly patterns move spatially in time.

4.2.1. Energy Reservoirs

Figures 4a–4d show P_m (integrated over depths of 100–1,500 m) averaged over *D* as well as the anomalies of the phases $A - C$ with respect to *D*. The *D*-mean P_m distribution (Figure 4a) is largely similar to the results shown by Wu et al. (2017) and Hogg et al. (2017). Noting the logarithmic color scale, this figure shows that the dominant storage of P_m occurs at high latitudes around Antarctica, where dense water can be found close to the surface; this water contains energy that is available to be converted to KE by sinking through the depth of the ocean to its reference level. At low latitudes, P_m is orders of magnitude smaller but still nonzero in regions where fluid is lighter than the reference state. Moreover, P_m has a strong gradient across the ACC, and large values of P_m can be found in the subtropical regions.

The P_m-anomalies related to the phases *A* and *C* are mostly located in the regions of dominant P_m around Antarctica, especially within the WGKP region (Figures 4a–4d). A strong positive anomaly west of the Kerguelen Plateau emerges in *A*, intensifies in *B*, and then fades out as a positive anomaly along the boundary current of the Weddell Gyre. Moreover, a significant negative anomaly is situated in the Atlantic part of the SO and also peaks in *B*. A dipole pattern of anomalies is also found in Hogg et al. (2017) for their simulations in which convection is triggered. In contrast, in simulations with only increased winds (and no convection triggered)

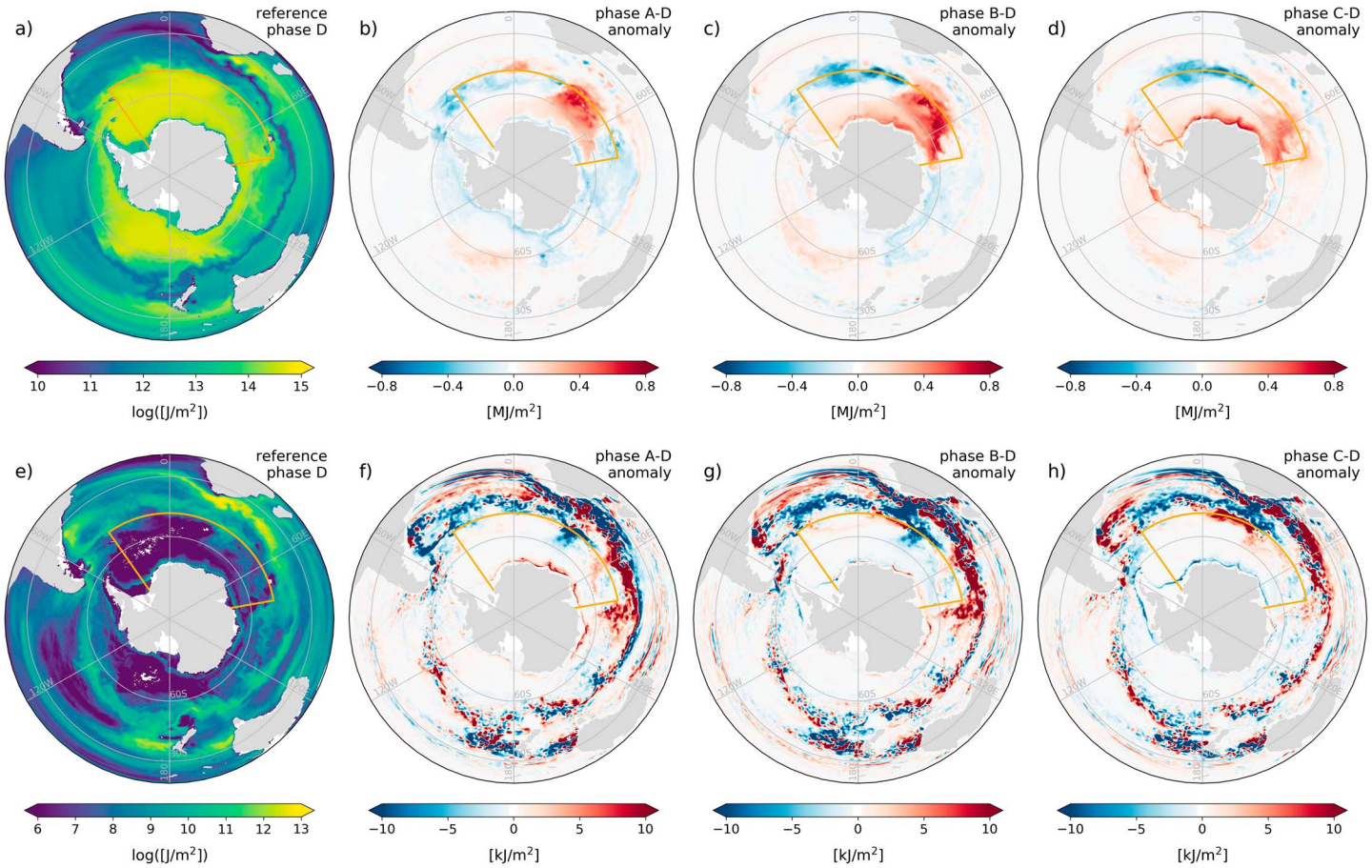

Figure 4. (a–d) P_m integrated from 104.2 to 1,501.2 m for the reference phase *D*, as well as the anomalies with respect to the reference phase of the phase of increasing convection *A*–*D*, full convection *B*–*D*, and decreasing convection *C*–*D*. (e–h) P_e integrated from 104.2 to 1,501.2 m for *D*, *A*–*D*, *B*–*D*, and *C*–*D*.

dipole type anomalies are absent (Hogg et al., 2017; Wu et al., 2017). The changes in the P_m distribution may be related to the onset of convection (described in subsection 3.2), subsequently induced changes in the slopes of the isopycnals (reflected in ACC, upper and lower MOC transport changes), and Antarctic shelf dynamics.

Figures 4e–4h show P_e (integrated over depths of 100–1,500 m) averaged of *D* as well as the anomalies of the phases *A*–*C* with respect to *D*. Again, the *D*-mean distribution of P_e is similar to the results presented by Wu et al. (2017). Generally, one can observe the tendency that regions of large P_m are related to relatively small P_e and vice versa. This holds for both the *D*-mean and the anomalies related to the phases *A*–*C*. That is, in the region of dominant P_m storage at high latitudes around Antarctica, in particular with in the WGKP region, both the *D*-mean and the anomalies of P_e are small. Large values of P_e anomalies are found in the main ACC and the Agulhas retroflection regions, particularly where minimum values of P_m are found. The anomalies of P_e exhibit a form of large-scale pattern with mainly positive (negative) anomalies in the Indian (Atlantic) part of the SO. The anomalies are related to changes in eddy activities.

Figures 5a–5d show K_m (integrated over depths of 100–1,500 m) averaged of *D* as well as the anomalies of the phases *A*–*C* with respect to *D*. The *D*-mean K_m distribution is similar to the results presented previously by von Storch et al. (2012) and Wu et al. (2017). Strong kinetic energies are concentrated in sharp boundary currents and narrow filaments in the SO that form the ACC. Most of the narrow filaments are along the zonal direction and indicate narrow zonal jets. The strength of the ACC varies notably as it flows eastward. In the region of the subpolar gyres (in particular in the WGKP region) K_m is smaller with the largest values related to the boundary currents of the subpolar gyres. The anomalies of K_m are mainly located in the region of large *D*-mean K_m values, that is, predominantly in the main ACC region. In the subpolar gyres/WGKP region the K_m anomalies are relatively small. Moreover, there is no distinct large-scale pattern visible, but positive and

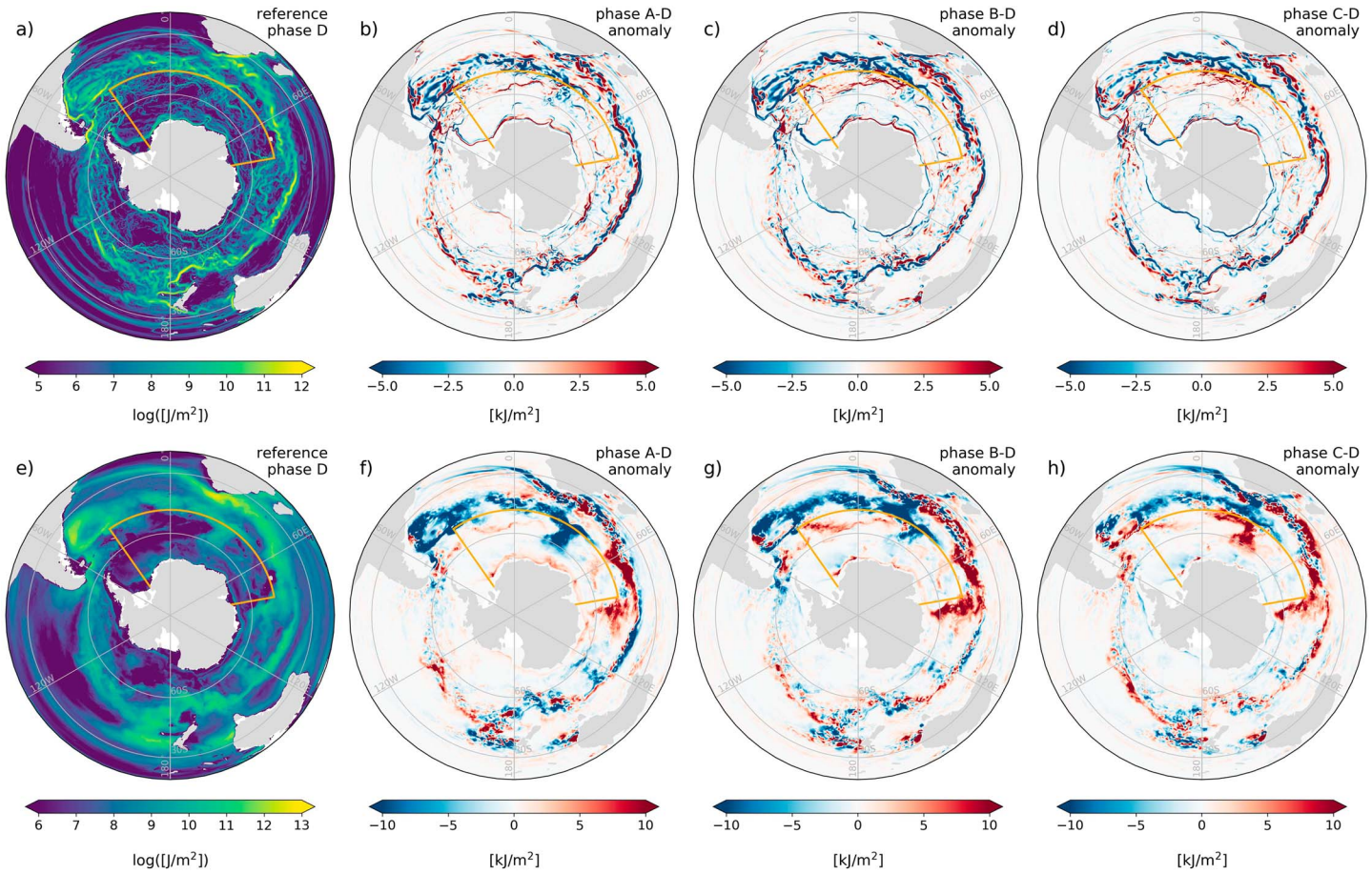

Figure 5. (a–d) K_m integrated from 104.2 to 1,501.2 m for *D*, *A*–*D*, *B*–*D*, and *C*–*D*. (e–h): K_e integrated from 104.2 to 1,501.2 m for *D*, *A*–*D*, and *B*–*D*, *C*–*D*.

negative anomalies are spatially close to each other and concentrate in some narrow bands. The anomalies are related to the meandering/shifting of the zonal flow/jets.

Next, Figures 5e–5h show K_e (integrated over depths of 100–1,500 m) averaged of *D* as well as the anomalies of the phases *A*, *B*, and *C* with respect to *D*. The *D*-mean K_e distribution is similar to the results shown by von Storch et al. (2012) and Wu et al. (2017). That is, similar to the *D*-mean K_m and P_e distributions large values in K_e are found in the main ACC region whereas in the subpolar gyres/WGKP region K_e is relatively small. In other words, the maxima of K_e are often located near the strong time-mean currents. These regions have strong mesoscale variability, due to barotropic and baroclinic instabilities. In contrast to the *D*-mean K_m distribution, that of K_e shows smoother spatial structures (similar to the *D*-mean P_e distribution). The smoothness indicates a large variability in the positions of the mesoscale eddies and other transient features.

The anomalies of K_e resemble those of P_e (and not the anomalies of K_m) in being more evenly spread over the SO instead of being concentrated in some narrow bands. That is, significant anomalies of K_e are found in the main ACC and the Agulhas retroflection regions. The anomalies of K_e exhibit a form of large-scale pattern with mainly positive (negative) anomalies in the Indian (Atlantic) part of the SO. At high latitudes around Antarctica, in particular with in the WGKP region, the anomalies of K_e are mostly small.

In summary, large *D*-mean values and anomalies are mainly found at high latitudes (WGKP region) for P_m whereas for K_m, P_e, K_e large *D*-mean values and anomalies are mainly found in the main ACC and the Agulhas retroflection regions. Moreover, for P_m, P_e, K_e the anomalies exhibit large-scale patterns whereas the anomalies of K_m are more scattered. Hence, P_e and K_e are very similar (which is also stated by Wu et al. (2017) and explained here by a PV balance).

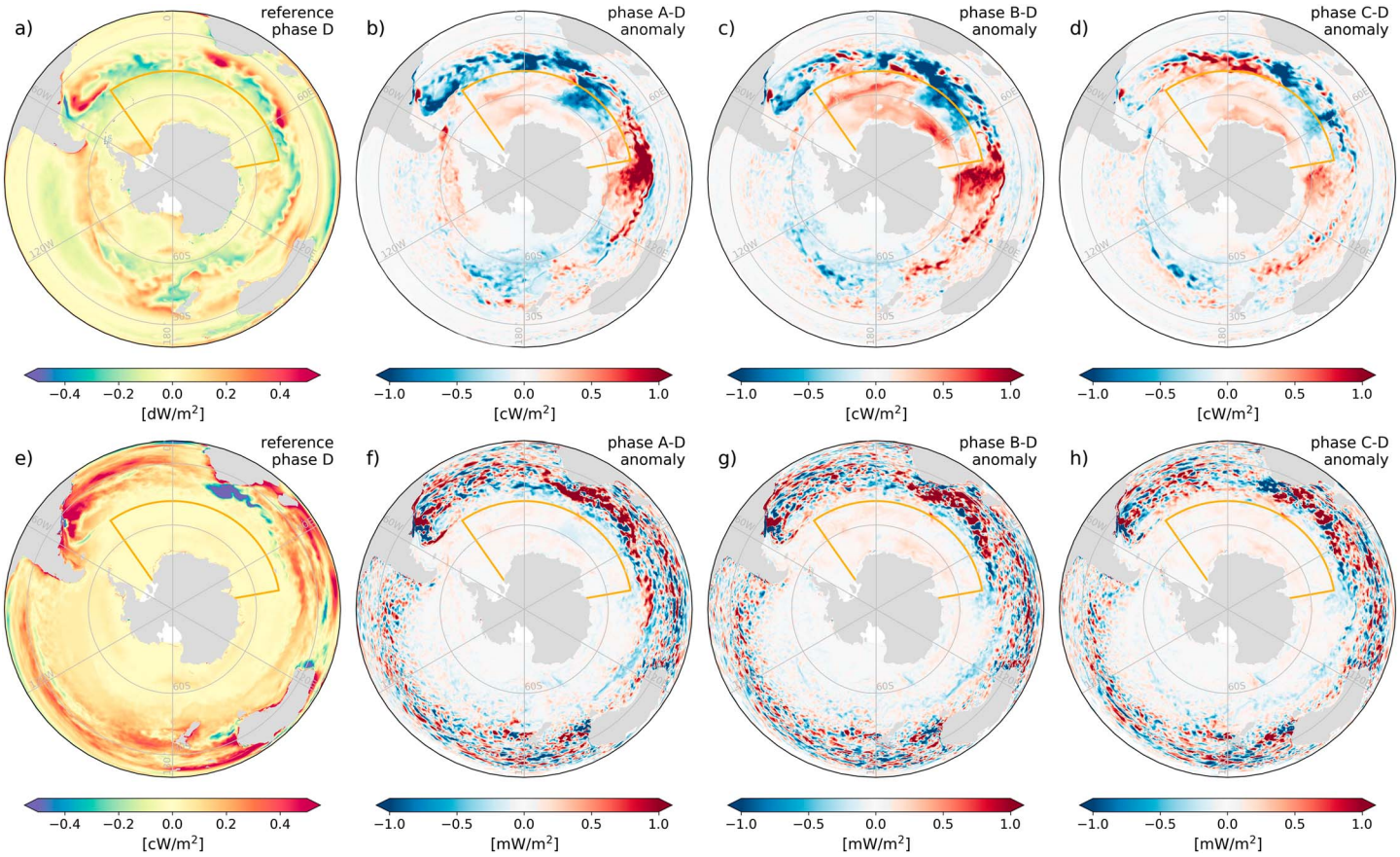

Figure 6. (a–d) $G(P_m)$ at the surface for *D*, *A*–*D*, *B*–*D*, and *C*–*D*. (e–h) $G(P_e)$ at the surface for *D*, *A*–*D*, *B*–*D*, and *C*–*D*.

4.2.2. Generation of Available Potential and KE

Figures 6a–6d show the mean power input via buoyancy fluxes ($G(P_m)$) averaged over *D* as well as the anomalies of phases *A*–*C* with respect to *D*. The generation of P_m by the total buoyancy flux averaged over *D* is negative over most of the SO and positive in the Antarctic marginal seas and at lower latitudes. Moreover, strong positive signals in $G(P_m)$ are found in the Argentine Basin as well as the Agulhas retroflection region. This pattern is broadly similar to what is found in previous studies (von Storch et al., 2012; Wu et al., 2017).

More interestingly, the anomalies related to phases *A*–*C* show a clear large-scale pattern. In the WGKP region a positive signal starts to emerge during *A*, reaches its maximum during *B*, and diminishes during *C*. This signal is obviously related to the deep convection (i.e., anomalous cooling at the surface). Moreover, in the Indian Ocean sector of the SO east of the Kerguelen Plateau, a strong positive anomaly is present during *A*–*B*, which diminishes during *C*. To the west of the Kerguelen Plateau up to Drake Passage and north of the Weddell Gyre a strong negative anomaly is present during *A*–*B*, which diminishes and incorporates positive anomalies during *C*. Finally, in the Pacific the anomalies are rather small. That is, the anomalies of $G(P_m)$ comprise the different large-scale anomaly patterns seen for P_m (in the WGKP region), on the one hand, and for P_e and K_e (in the main ACC region), on the other hand.

Figures 6e–6h show the eddy power input via buoyancy fluxes ($G(P_e)$) averaged over *D* as well as the anomalies of phases *A*–*C* with respect to *D*. The values for the *D*-average are very small in the SO. The anomalies for phases *A*–*C* are very noisy and, hence, do not depict a coherent pattern of large-scale low-frequency variability.

We note that the spatial patterns of both $G(P_m)$ and $G(P_e)$ (mean and anomalies) are dominated (not shown) by the respective heat flux component (i.e., heating [cooling] relatively light [heavy] water masses). However, in an integral positive and negative values cancel each other such that for the integrated values of the buoyancy power input the freshwater flux components become crucial as well. For example, for integration up to 30°S

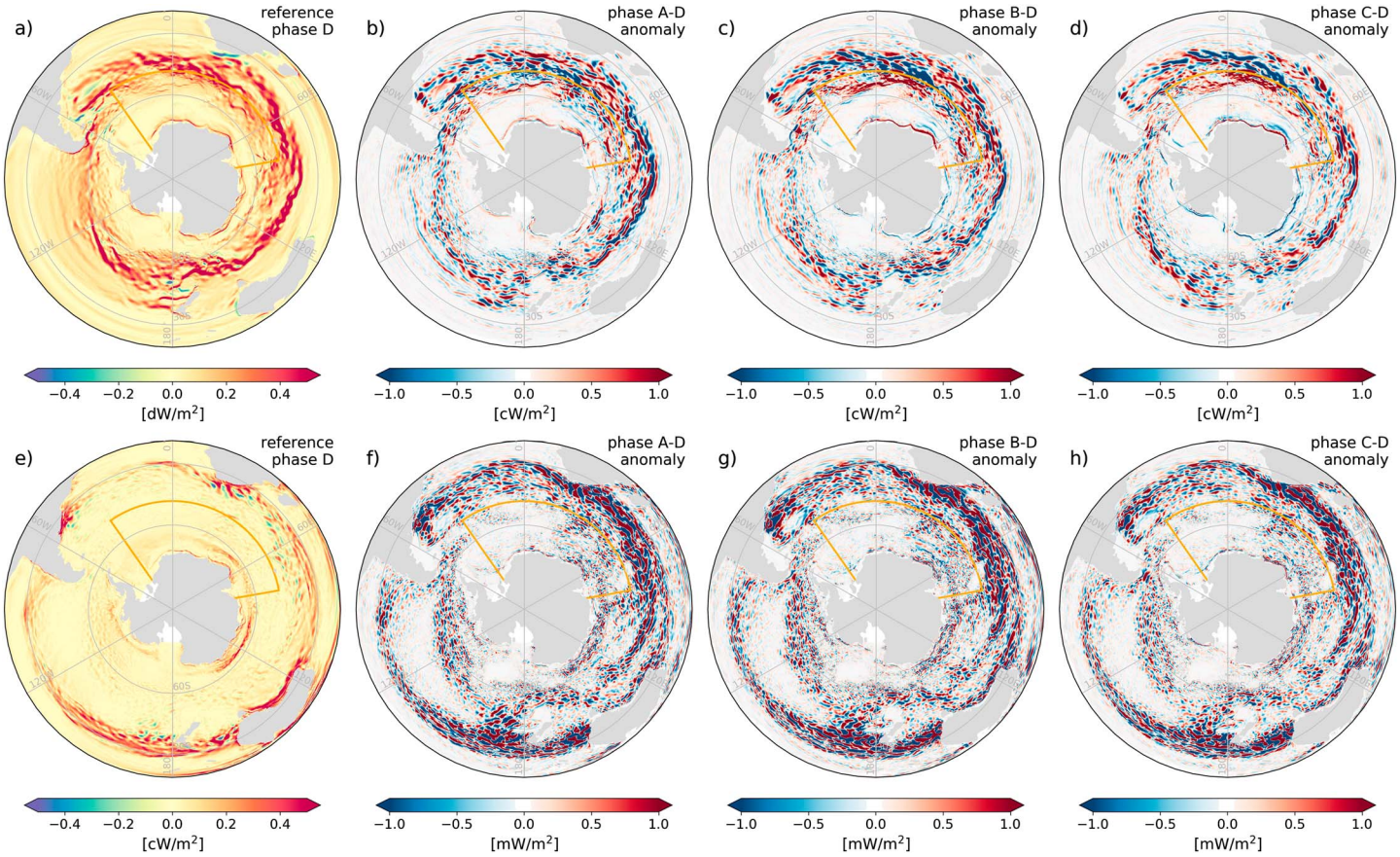

Figure 7. (a–d) $G(K_m)$ at the surface for D, $A-D$, $B-D$, and $C-D$. (e–h) $G(K_e)$ at the surface for D, $A-D$, $B-D$, and $C-D$.

(see also Figure 3b) the heat flux component of $G(P_m)$ ($G(P_e)$) is related to a power input of 148 GW (81 GW) whereas the freshwater component is related to a power input of −205 GW (−13 GW).

Finally, Figure 7 shows the power input by the winds ($G(K_m)$ and $G(K_e)$, respectively) averaged of D as well as the anomalies of the phases $A-C$ with respect to D. The geographic distribution of the D-average of the generation from the time-mean wind stress resembles the distributions described in previous studies (Hogg et al., 2017; von Storch et al., 2012; Wu et al., 2017). That is, the power input from the time-mean wind stresses is most intense in the region of the eastward flowing ACC where the westerly winds are strongest with generally larger magnitudes south of Africa and in the Indian Ocean sector of the SO than those farther eastward. In contrast, the D-average of $G(K_e)$ is relatively small in the entire ACC region compared to previous studies since in our simulation a wind stress climatology is used (instead of 6-hourly winds as in von Storch et al., 2012, or Wu et al., 2017). The anomalies of both $G(K_m)$ and $G(K_e)$ for phases $A-C$ are strong in the main ACC region and weaker in the subpolar gyres. Positive and negative anomalies are concentrated in narrow bands next to each other and, hence, do not depict the pattern of a large-scale low-frequency variability.

In summary, $G(P_m)$ comprises the large-scale anomaly patterns found in the reservoirs P_m, P_e, K_e, whereas the anomalies of $G(K_m)$, $G(K_e)$, $G(P_e)$ are rather noisy and do not exhibit patterns of a large-scale low-frequency variability.

4.2.3. Conversions Between the Four Energy Reservoirs

Figures 8, 9 show the four energy conversion terms $C(P_m, K_m)$, $C(P_e, K_e)$, $C(P_e, P_m)$, $C(K_e, K_m)$ (integrated over depths of 100–1,500 m) averaged of D as well as the anomalies of phases $A-C$ with respect to D. For all conversion terms it holds that they are dominated by smaller scale structures of positive and negative values (similarly to the previous studies: Hogg et al., 2017; von Storch et al., 2012; Wu et al., 2017). Consequently, only in an integrated sense a sign/direction can be associated with each of the conversions. Moreover, the anomaly patterns largely resemble that of the respective mean pattern. Hence, none of the conversion terms depicts anomaly patterns of a large-scale low-frequency variability. The conversions $C(P_m, K_m)$ and $C(P_e, K_e)$ (the latter

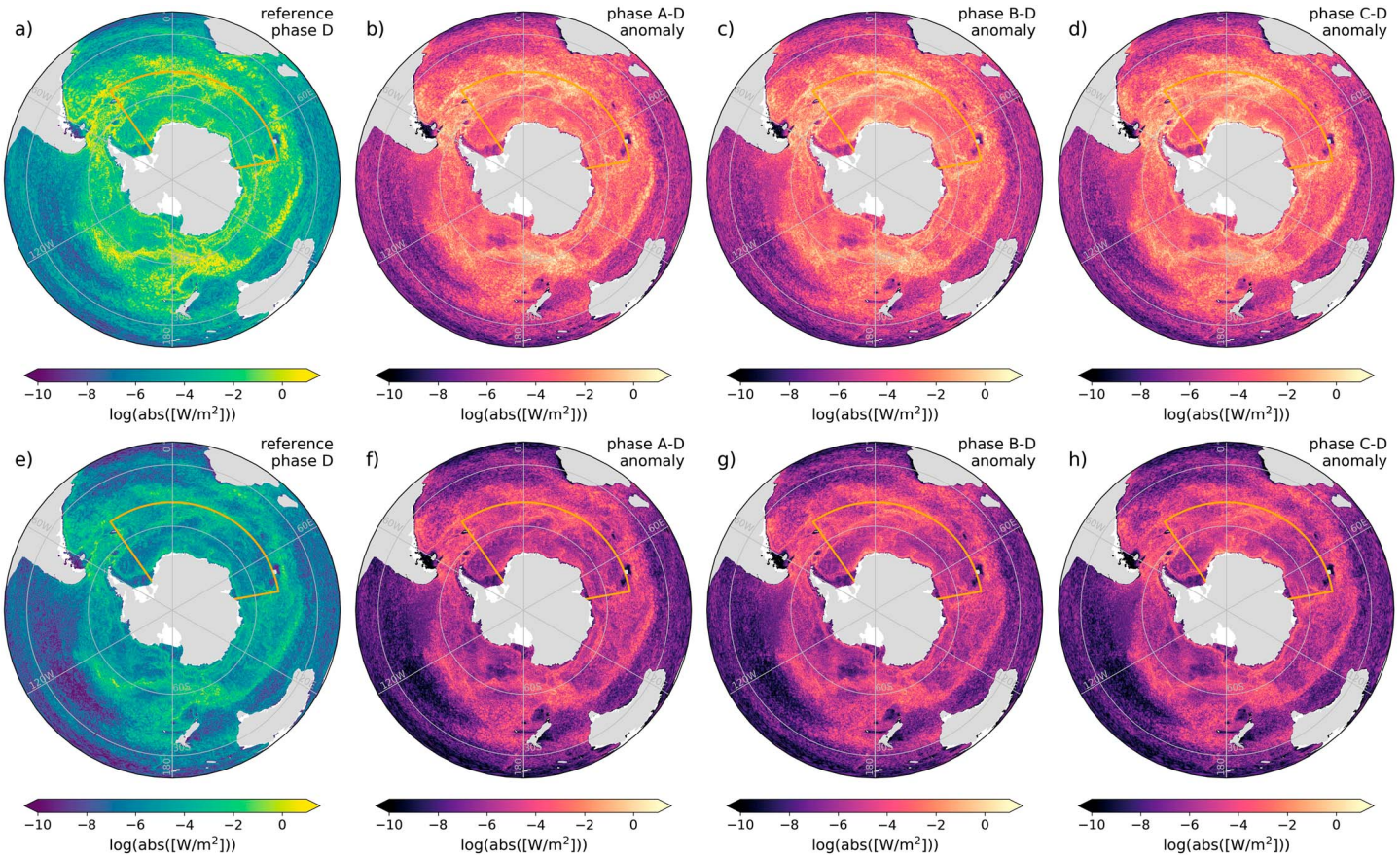

Figure 8. (a–d) $C(P_m, K_m)$ integrated from 104.2 to 1,501.2 m for *D*, *A*−*D*, *B*−*D*, and *C*−*D*. (e–h) $C(P_e, K_e)$ integrated from 104.2 to 1,501.2 m for *D*, *A*−*D*, *B*−*D*, and *C*−*D*.

measuring the strength of the baroclinic production) exhibit significant values in the entire SO, including the subpolar gyres (within the WGKP region). In contrast, the conversions $C(P_e, P_m)$ and $C(K_e, K_m)$ (the latter being related to barotropic instabilities) only exhibit significant values in the main ACC, Agulhas retroflection, and boundary current regions.

A reason for the fact that the spatial patterns of the conversion terms are largely insensitive to the low-frequency variability might be that the conversions are strongly influenced by the large topographic features (see, e.g., Wu et al., 2017, for details). Apparently, in the SO the relaxation of isopycnal surfaces is mainly through the processes associated with large topography features ("topography-induced meanders"; Bischoff & Thompson, 2014; Chapman et al., 2015; Thompson & Naveira Garabato, 2014).

4.3. Time Series of Spatially Integrated LEC Terms

In this section we look at the variability of the different LEC terms from another angle by considering the actual time series of the spatially integrated LEC terms. However, an integrated energy balance does not provide a completely disentangled breakdown of the individual components of the energy budget due to integration over numerous processes. This also implies some sensitivity to the choice of integration region since positive and negative anomalies can compensate each other differently depending on the chosen integration region. In particular, even SO30 is still a rather large region, implying the presence of numerous processes as well as numerous positive and negative anomalies (see Figures 4–9) such that the corresponding time series can be quite irregular for certain LEC terms. For that reason we will mainly focus on the WGKP region in this section. Moreover, since the temporal averages and standard deviations are discussed in section 4.1, we present standardized time series here; that is, for each quantity q we consider $Q = (q - \bar{q})/\sigma_q$ such that the mean $\bar{Q} = 0$ and the standard deviation $\sigma_Q = 1$. The corresponding nonstandardized time series are given in the auxiliary material (see Figures S2 and S3). Finally, in order to ease comparison, we show the curve of the maximum MLD (indicating convection) in each plot as a reference.

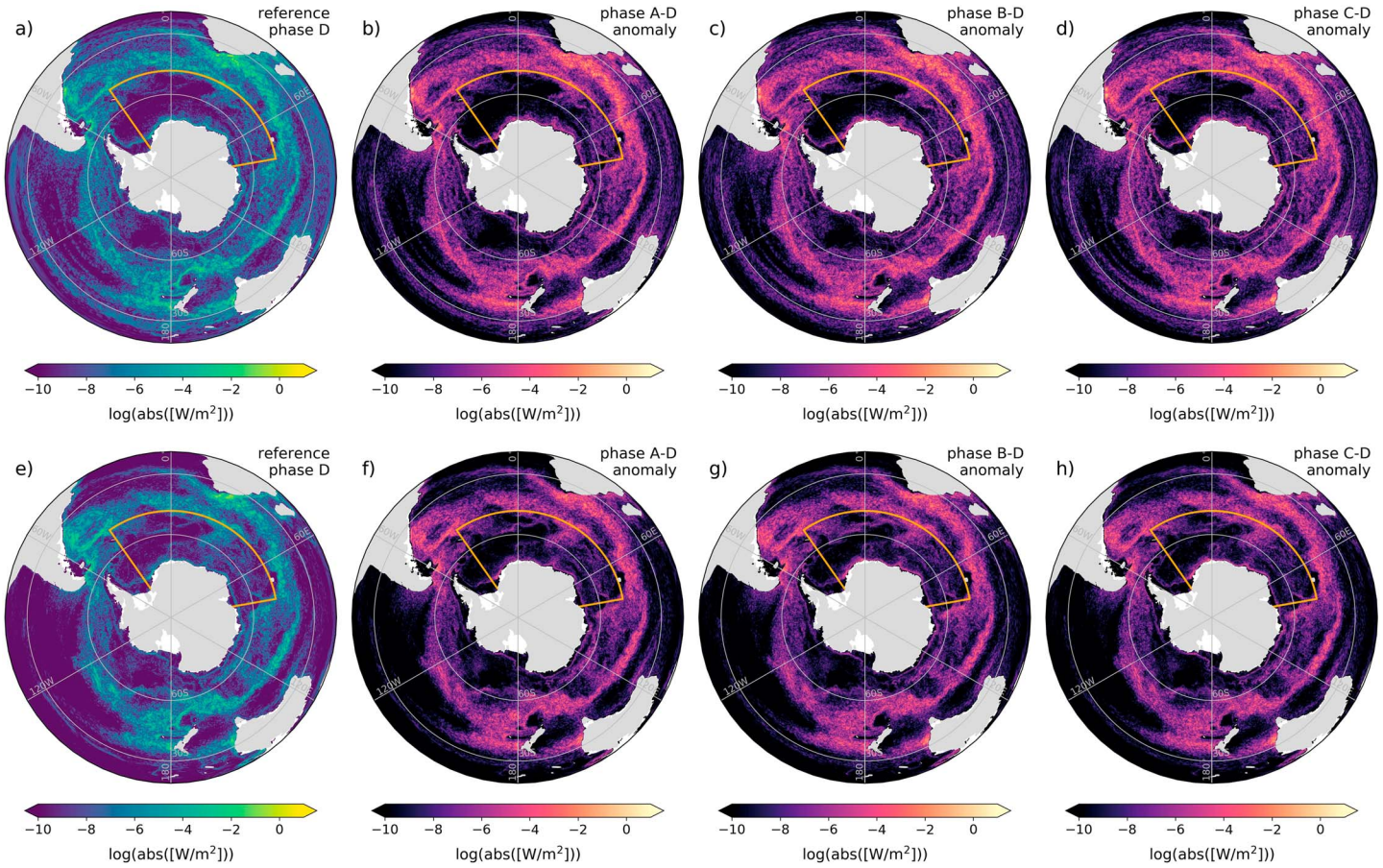

Figure 9. (a–d) $C(P_e, P_m)$ integrated from 104.2 to 1,501.2 m for D, $A-D$, $B-D$, $C-D$. (e–h) $C(K_e, K_m)$ integrated from 104.2 to 1,501.2 m for D, $A-D$, $B-D$, and $C-D$.

Figure 10a shows the different power inputs integrated over the WGKP region. Convection (upwelling of anomalous warm/light waters and sinking of anomalous cold/heavy waters) is associated with strong buoyancy loss (heat flux driven due to anomalous cooling at the surface) and hence APE generation from surface buoyancy flux (see also Figures 6a–6d). Correspondingly, $G(P_m)$ (blue) is largely in phase with MLD. The wind power input $G(K_m)$ (red, with a variance similar to $G(P_m)$, Figure 3c) is slightly lagged with respect to $G(P_m)$ reaching its maximum value a few years later. Since the wind field is prescribed in our simulation the changes in wind power input must be related to a reorganization of the flow field, for example, meridional shifts of the ACC and related changes in the extension of the Weddell Gyre. The mean $G(P_e)$ term is about an order of magnitude smaller than its standard deviation (see Figure 3c). The term $G(P_e)$ (cyan) is largely in phase with both MLD and $G(P_m)$. In the WGKP region these two terms are in phase due to the common heat release/cooling of surface waters during convection. In the SO30 region, both terms compensate each other approximately, but the spatial scales are very dissimilar, indicating different underlying processes (changes in MOC vs. mesoscale eddies). On the other hand, $G(K_e)$ (magenta) is essentially anticorrelated with MLD and also with $G(K_m)$. However, $G(P_e)$ and $G(K_e)$ in the WGKP region have relatively small mean values and variances (see Figure 3c) and, hence, play a minor role in the multidecadal variability within the WGKP region (see also Figures 6e–6h and Figures 7e–7h).

Figure 10b shows the different energy reservoirs integrated within the WGKP region. The mean energy reservoirs P_m (blue) and K_m (red) are phase-wise largely in accordance with the corresponding power input terms $G(P_m)$ and $G(K_m)$, respectively. That is, an increase in $G(P_m)$ ($G(K_m)$) is accompanied by an increase in P_m (K_m) with K_m being slightly lagged with respect to P_m. In contrast, the eddy energy reservoirs P_e (cyan) and K_e (magenta) are out of phase with respect to $G(P_e)$ and $G(K_e)$, respectively. This indicates again that P_e and K_e in the WGKP region are not driven by their power input terms but by conversion and boundary terms (see Figure 3c).

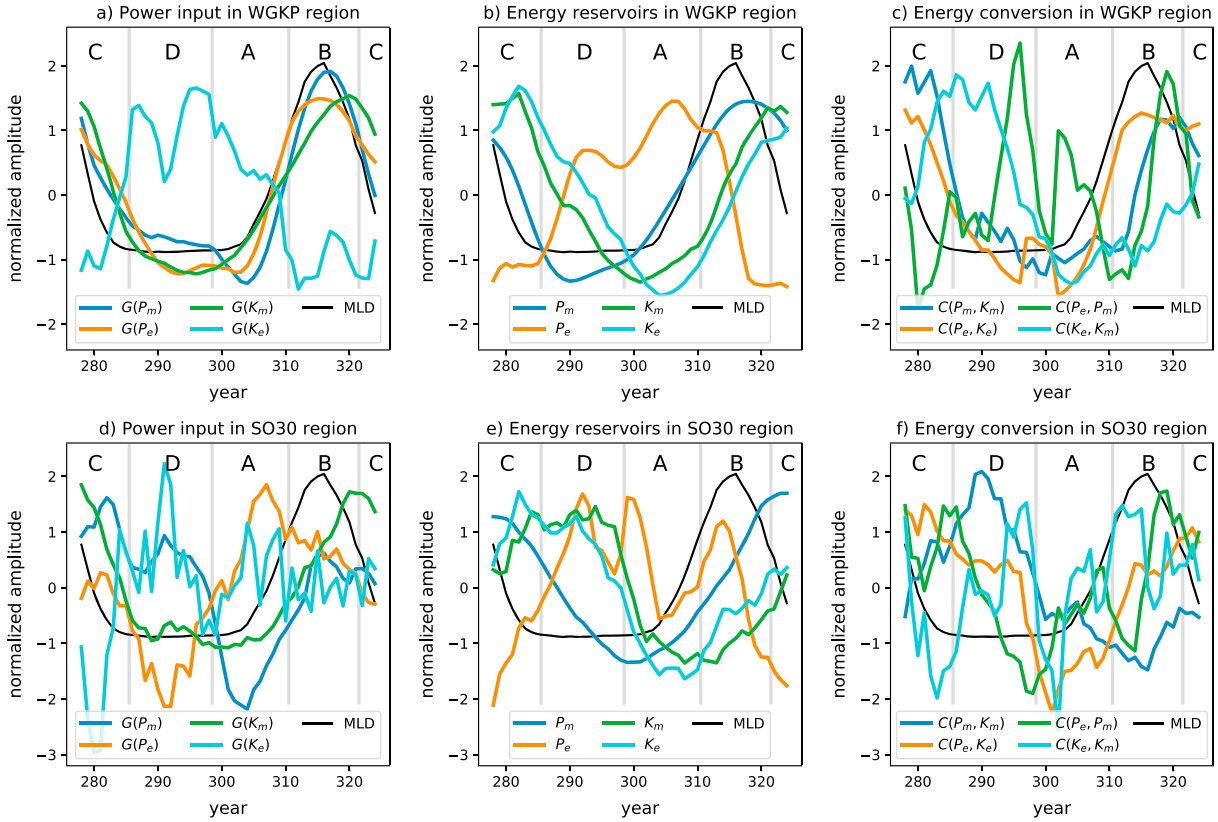

Figure 10. (a–c) Normalized time series of LEC terms integrated over the WGKP region. (d–f) For comparison, also, LEC terms integrated over the SO30 region are shown. Mean and standard deviation values can be found in Figures 3b and 3c. In all plots the black line (MLD) represents the normalized time series of the maximum mixed layer depth in the Weddell Gyre, which indicates convection. The reference phase (*D*), the phase of strong convection (*B*), and the transition phases (*A*, *C*) are also indicated. LEC = Lorenz energy cycle; MLD = mixed layer depth; WGKP = Weddell Gyre to Kerguelen Plateau.

Figure 10c shows the different energy conversions integrated within the WGKP region.

Physically, convection induces vertical velocities that are correlated with potential density anomalies and hence would contribute to the $C(P_m, K_m)$ exchange term. However, since the POP simulation employs the KPP mixing scheme that parametrizes convection as enhanced mixing (see section 3.2), there are no vertical velocities directly associated with convection in POP. This complicates the interpretation of the $C(P_m, K_m)$ term. Convection changes the potential density field (including horizontal density gradients) and influences the overturning circulation. Interpreting the normalized time series, one must further note that $C(P_m, K_m) < 0$ at all times in all considered regions. In the WGKP region, both $C(P_m, K_m)$ (blue) and $C(P_e, K_e)$ (red) are largely in phase with MLD. Furthermore, $C(P_m, K_m)$ is not contributing to the increase in P_m but $C(P_m, K_m)$ is balanced by (i.e., anticorrelated with) the lateral boundary transport of K_m (see Figure 3c and section 5.3; see also Figures S2 and S3). Moreover, $C(K_m, K_e)$ (magenta) lags K_e whereas $C(P_e, K_e)$ leads K_e, which again suggests that $C(P_e, K_e)$ is responsible for the increase in K_e as well as the decrease in P_e. Finally, the variability in $C(P_m, P_e)$ (cyan) is rather irregular but has a small variance anyway (see Figure 3c).

For comparison, we also show the power input, energy reservoirs, and energy conversions integrated within SO30 in Figures 10d–10f. The variability of $G(K_m)$, $G(P_m)$, $C(P_e, K_e)$ is largely similar for integration within both SO30 and WGKP. However, for P_m, K_m, K_e, $G(P_e)$, $C(P_m, K_m)$ significant phase differences appear, and, moreover, P_e, $G(K_e)$, $C(P_m, P_e)$, and $C(K_m, K_e)$ do not show a clear multidecadal cycle anymore. That is, while integrating the LEC terms within the WGKP region still offers a largely consistent dynamical picture with respect to convection, the integration of the LEC terms within the SO30 probably includes other processes such that relationships become less clear. In particular, it holds that $C(P_m, K_m)$ and MLD are anticorrelated such that for the integral within SO30 it does not hold that deep convection is associated with destruction of APE. We offer two possible dynamical interpretations of these results in the next section.

5. The Mechanism of the SOM

In this section, we start by summarizing the initial description of the SOM by Le Bars et al. (2016; section 2.2) and develop this perspective further with our more comprehensive LEC analysis (section 5.2), which is followed by a discussion of the role of convection (section 5.3).

5.1. The Initially Proposed Mechanism

Le Bars et al. (2016) presented a preliminary description of the energetics of the SOM by employing baroclinic instability and eddy-mean flow interactions as a dynamical framework (following Hogg & Blundell, 2006) using the total PE and KE. With reference to their Figure 4, the energetics of a SOM cycle was divided into the following four phases: Phase *A* represents a state of low total energy starting at the minimum in PE and ending at the minimum in KE. The storage of PE is small in this regime, so the production of baroclinic eddies is weak. In phase *B*, PE builds up until the maximum in PE is reached. This is because the flow is accelerated zonally by the wind stress. Phase *C* represents a state of high total energy starting at the maximum in PE and ending at the maximum in KE. The flow exceeds a critical threshold for enhanced baroclinic instability, which induces an increased generation of eddies by the mean flow. The PE that was stored during phases *A* and *B* is transferred to KE. The enhanced turbulence rearranges the flow field such that there is a loss of correlation between surface ocean velocity and wind stress. Therefore, energy input by the wind stress quickly decreases in regime *C*. Finally, phase *D* is defined by decreasing PE and KE. The storage of PE is exhausted so that the conversion of PE to KE begins to abate as well. This is combined with the reduction in energy input by the wind stress forcing and the system returns to its low-energy state (phase *A*).

As mentioned in section 4.2, since the phases *A*, *B*, *C*, and *D* correspond well to increasing, full, decreasing, and absent convection, respectively, we adopt the same terminology in this study.

5.2. The Eddy-Mean Flow Interaction Perspective

To connect the physical view of the evolution of the SOM to the different LEC terms, we have to consider (i) the temporal phasing of the different terms (which follows from Figure 10) and (ii) the relative magnitude of each term (which follows from Figure 3). In the relative phases of the terms, we still see aspects of the mechanism as presented in Le Bars et al. (2016). In the SO30 region, which captures the complete SOM signal, and the WGKP region, which captures the convective aspects, potential and KE reservoirs have low content in phase *A* (year 305) and the values increase up to phase *B* at year 320 (Figures 10b and 10e). This is occurring simultaneously with an increase in $G(K_m)$, in agreement with the view that the mean flow is accelerated by the wind (Figures 10a and 10d). The mean and standard deviation values of $G(K_e)$ are significantly smaller, and hence, their phase in Figures 10a and 10d is not relevant.

From phases *A* to *C*, the SST-based SOM index switches from negative to positive (Figure 1a), as cold anomalies appear in the WGKP region. These erode the density stratification and induce convection (vertical mixing), as shown here through the mixed layer deepening in all Figures 10. As will be discussed in the next section, the transient behavior of $C(P_m, K_m)$ does not directly respond and cannot be explained by the increase in deep convection itself but is governed by the overturning response to the change in deep convection. At the end of phase *B* and toward phase *C*, the baroclinic pathway sets in as the conversion term $C(P_e, K_e)$ becomes maximal positive, indicating a conversion of potential to KE during the instability process (Figure 10f). This leads to a less zonal jet, which decreases the input of energy input by the wind $G(K_m)$ (Figure 10d).

As the SOM index becomes negative again during phase *C*, warm anomalies are present in the WGKP region, and a stable stratification is obtained, the mixed layer shallows, and the conversion term $C(P_m, K_m)$ is maximal at minimum MLD, that is, less negative (Figure 10c). Simultaneously, the dissipation decreases, and the decrease in P_m is mostly due to the weakening of the horizontal density gradients due to the baroclinic instability process (Figure 10e). This will lead to a decrease in eddy formation, and hence, the conversion term $C(P_e, K_e)$ decreases (Figure 10f), decreasing also the reservoir energy content K_e (Figure 10e). The LEC in the WGKP region shows a similar phasing of the terms although it is less clear because of a stronger role of the boundary terms (Figures 10a–10c).

Hence, it is timing of the baroclinic pathway $C(P_e, K_e)$ and the input of the energy by the wind $G(K_m)$ that confirm that the mechanism suggested in Le Bars et al. (2016) is correct. This view was based on the results in Hogg and Blundell (2006), which were obtained for a three-layer quasi-geostrophic model. However, we cannot separate out the role of bottom topography (identified to be crucial in Hogg & Blundell, 2006) because the bottom form stress effects are not explicitly computed in the LEC (they are included in the residual

dissipation term). What confuses this view is the occurrence of strong convection associated with the buoyancy anomalies generated through the propagation of the spatial pattern of the SOM. Although the effects of convection appear to phase very well with a relatively large conversion term $C(P_m, K_m)$, in particular on regional scale of the WGKP, this convective mixing is caused by the SOM and does not take part in the increase of the baroclinic pathway due to enhanced dissipation.

5.3. The Convection and Overturning Perspective

The presence of open ocean deep convection in the Weddell Sea, with a variability that phases very well with the SOM, enables an alternative view of the SOM in which the stimulation of convection could be an essential part of the mechanism instead of just being a side effect. In noneddying ocean and climate models the following convection-restratification type of mechanism has been described (Dijkstra & der Heydt, 2017; Latif et al., 2013; Martin et al., 2013; Winton, 1995): The deep convection is induced by a strong accumulation of heat at middepth, which leads to a destabilization of the water column. The convection shuts down when the heat reservoir at middepth is virtually depleted (possibly accompanied by strong freshening event at the sea surface). The heat originates from relatively warm deep water formed in the North Atlantic such that the open ocean deep convection is essentially due to the inflow of warm NADW into the Atlantic-Indian Ocean Basin at middepth. Moreover, the westward return flow in the southern part of the Weddell Gyre effectively transports heat into the Weddell Sea where it is eventually "trapped" in the gyre circulation. Consequently, the several decades lasting recharge process of the heat reservoir depends on the AMOC and the Weddell Gyre and sets a minimum delay for the deep convection to recur. Additionally, the sea-ice characteristics can have a significant regulating effect.

The impact of the deep convection variability in the Weddell Sea on the ocean circulation as found in our simulation (see Figure 1 described in section 2) is similar to the results for noneddying ocean and climate models (Latif et al., 2013; Martin et al., 2013): The shutdown of the deep convection yields a decline in the northward transport of AABW whereas its onset causes an increase (green, Figure 1b). In contrast, the southward NADW transport increases during the nonconvective regime (supporting the accumulation of heat in the Weddell Gyre) and decreases during deep convection (purple, Figure 1b). These effects are lagged with respect to the convection MLD signal such that southward NADW transport peaks and northward AABW transport is at its lowest at the onset of convection because the density anomaly has to propagate from their source region to the western boundary of the South Atlantic to induce a geostrophic response in the overturning cells. Moreover, the ACC strength is decreased during the nonconvective regime and increased during the convective regime (orange, Figure 1a). This is related to the impact of the deep convection on the pressure gradient across the ACC. When no convection takes place the cold waters south of the ACC gradually warm between 200- and 2,000-m depth (Figure 2b), and the front across the ACC weakens. As a result, the ACC weakens as well (orange, Figure 1a). When convection peaks, the heat is suddenly released, and the waters south of the ACC front cool (Figure 2b). As a result, the ACC strengthens with a small lag of about 5 years.

The convection-overturning perspective of the SOM is supported by the following quantitative properties of the LEC in both the Southern Ocean as a whole and the WGKP area in particular (see Figures 3b and 3c): The variations in energy conversion are dominated by $C(P_m, K_m)$, and in the K_m energy budget this term is balanced by advection across the boundary of either region (see Figures S1–S3). In the P_m budget, variations in $C(P_m, K_m)$ are balanced by the combination of cross-boundary advection and dissipation. Here and in the eddy energy budgets the advective terms cannot be estimated, as their calculation requires triple correlations that were not computed. However, from the relative smallness of variations in the globally integrated dissipative terms (Figure 3a), we infer that it is most likely that the variations in the D/B terms in Figures 3b and 3c are dominated by variations in boundary advection (B) as well. This picture is completely consistent with the link between variations in deep convection in the Weddell Sea and variations in the deep overturning cell in the Southern Ocean, with northward transport of AABW and southward transport of NADW (Figures 1b and 2).

On the other hand, the phase relation of the LEC terms and convection is difficult to interpret. Normally deep convection is associated with destruction of APE (Hogg et al., 2017), but here the opposite occurs when considering the entire Southern Ocean where convection coincides with a peak in P_m. For the WGKP region this phase relation still partly holds, and a minimum of P_m is found at the onset of convection. This inconsistency is due to the nonlocal nature of the APE calculations where the global area average density profile is taken to be the minimum PE state. This simplification breaks down in convection regions, and other concepts need to be applied, such as the convective APE (Su et al., 2016a).

During deep convection $C(P_m, K_m)$ is at its minimum (Figures S2 and S3). In the LEC framework the energy conversion is due to vertical advection and not to convective mixing (see equation (11)). However, the link between convective mixing and net sinking of dense water or upwelling of less dense water is far from straightforward (Spall & Pickart, 2001), especially given that the employed KPP scheme parametrizes convection as enhanced mixing only. Here the change in $C(P_m, K_m)$ might be explained by the changes in meridional overturning and density anomalies. When deep convection peaks, the (upper) NADW cell (clockwise in a latitude-depth overturning stream function plot) is anomalously strong, and the (lower, anticlockwise) AABW cell is anomalously weak. Together, they combine to a full depth and Southern Hemisphere basin-wide clockwise overturning cell (see Figure S4). The overturning cells slightly lead the convection by a few years, but they do correlate (deep cell) and anticorrelate (upper cell) with the mean potential to KE conversion (Figures 1b and 10c). So during deep convection upwelling of Central and North Atlantic Deep Water is enhanced at subpolar latitudes, and downwelling of AABW is anomalously weak. This anomalous net upwelling is mass compensated by anomalous net downwelling of lighter water north of 30°S. The signature of this anomalous overturning consists of a cross-hemispheric cell extending to the subpolar/subtropical gyre boundary in the Northern Hemisphere (Figure S4).

The opposite occurs when convection in the SO is weak. We observe a fixed-phase relationship with Southern Hemisphere overturning variability and changes in deep convection (the upper cell maximum leads convection by 8 years and the lower cell by 4 years; Figure 1b). As a result, the anomalous overturning interacts with the SO stratification leading to an oscillation in mean potential and KE (Figures 10b and 10e). When deep convection sets in, temperature drops, but salinity and density increase at 200- to 2,000-m depth, lagging deep convection by 4 years (Figure 2b). During this phase, the upper cell weakens. Fourteen years after convection peaks, the upper cell reaches a minimum and starts increasing again. When the upper cell gains strength the subsurface and middepth positive density anomaly decreases by enhanced upwelling of warm water. This keeps progressing until the stratification is destabilized by subsurface ocean warming at 200- to 2,000-m depth, and deep convection sets in again, stabilizing the vertical column by releasing the accumulated subsurface heat. The deep cell reacts in an opposite way and is in antiphase with the upper cell with a lag of 4 years.

6. Summary and Discussion

We studied the LEC associated with multidecadal spatiotemporal variability as found in a 326-year simulation with a strongly eddying version of the global ocean model POP. As the forcing in this simulation is only seasonal, clearly, this variability results from internal ocean mechanisms. Its spatial pattern has largest amplitudes in the Weddell Sea region of the Southern Ocean, and hence, it was referred to as the SOM. The study extends earlier ones (Hogg et al., 2017; von Storch et al., 2012; Wu et al., 2017) by looking at low-frequency variability of energy reservoirs and conversions instead of only those of (statistical) equilibrium states.

We showed that the order of magnitude of each of the production, reservoir, conversion, and dissipation/boundary terms of an equilibrium state agrees very well with values in von Storch et al. (2012) and Wu et al. (2017). This gives confidence that the analysis was done correctly even though part of the boundary and dissipation terms was not determined explicitly. The accordance of our results with the results of Hogg et al. (2017; who use a more sophisticated computation of the energetics because of a different reference state of minimal PE) also confirms the applicability of the LEC approximation used in this study.

The main aim of this paper was to provide more detail to the mechanism of the SOM as proposed by Le Bars et al. (2016) by considering the LEC, where both mean and eddy potential and KE reservoirs and their conversions were considered. We must admit that this turned out to be harder than we had originally anticipated because of the strong influence of convective processes in the variability. Hence, we offered two views on the SOM mechanism in section 5. In section 5.2 we show that the timing of the baroclinic pathway $C(P_e, K_e)$ and the input of the energy by the wind $G(K_m)$ are in agreement with the mechanism proposed in Le Bars et al. (2016). In section 5.3 we show that the effects of convection through the overturning may also be important for the existence of the SOM.

Many coarse resolution GCMs exhibit Southern Ocean open ocean convection with varying localizations and strengths (Heuzé et al., 2013), much in disagreement with observations in which the Weddell Polynya only appeared twice since the beginning of satellite observations (Scambos et al., 2018). In particular, Behrens et al. (2016) investigated the connection between open ocean convection and many Southern Ocean state

variables in the NIWA-UKCA model and a suite of CMIP5 models. These models differ in two significant ways from our model setup, on one hand they are not eddy resolving, and on the other hand they are coupled to both an atmosphere and an interactive sea ice model. In agreement with our results, they find a correlation between convection strength and Drake Passage transport and an anticorrelation between Drake Passage transport and Weddell Gyre strength (Figure 1). Also, the Kiel Climate Model exhibits episodic or periodic deep convection on centennial timescales in the Southern Ocean depending on the details of the sea ice model setup (Martin et al., 2013). In general, the simulation of open ocean convection in the Southern Ocean is highly sensitive to freshwater fluxes (precipitation, evaporation, glacial melt runoff, and transport by sea ice and icebergs), the sea ice model setup (affecting heat and salinity fluxes), and the employed mixing scheme through their effects on the stratification, both seasonally and on the long term (Behrens et al., 2016; Kjellsson et al., 2015; Stössel et al., 2015). In addition, mesoscale eddies can help restratify the deep ocean, enabling periodic deep convection (Carsey, 1980; Dufour et al., 2017). Comparing the convective events in the POP simulation with the two observed cases of open ocean convection in the Weddell Polynya, there is a marked difference in duration. In the POP simulation convection lasts some 15 years (Figure 2) while the observed Weddell Polynyas lasted three (Gordon, 1978) and two seasons, respectively. This difference between model and observations is likely caused by a combination of several factors influencing the buoyancy forcing of the POP model. For one, there is no coupled sea ice model, and consequently, the mean buoyancy forcing associated with sea ice that is included in the repeat monthly forcing fields remains the same for all years, independent of the presence of convection. More importantly, the use of restoring temperature conditions leads to very high heat flux anomalies in the order of 30 W/m^2 (cf. Figures 2c and 2d of Le Bars et al., 2016). When the high-resolution POP model is run coupled to an atmosphere and sea ice model in the Community Earth System Model (van Westen & Dijkstra, 2017), regular convective events continue to exist, but with a more realistic duration of approximately 4 years while the periodicity decreases to some 25 years (not shown).

The issue whether mesoscale eddies represent a necessary condition for the SOM (as suggested in section 5.2) or mesoscale eddies represent just another process that has a regulating effect on convective variability (next to, e.g., sea-ice characteristics) has to be left for future research. The LEC framework is targeted at the processes of baroclinic and barotropic instabilities. Moreover, it is based on the Lorenz APE, which involves the entire-domain-wide computation of a background density. Consequently, the LEC framework is not optimal in order to analyze convective processes and other concepts such as ocean convective APE (Su et al., 2016a), and eddy size-constrained APE density (Su et al., 2016b) may be helpful.

Acknowledgments

A. Jüling and H. A. Dijkstra acknowledge support by the Netherlands Earth System Science Centre (NESSC), financially supported by the Ministry of Education, Culture and Science (OCW), Grant 024.002.001. J. P. Viebahn acknowledges support by the Netherlands Organization for Scientific Research (NWO) through the Vidi project "Stochastic models for unresolved scales in geophysical flows," The POP simulations were performed on the Cartesius supercomputer at SURFsara (https://www.surfsara.nl) through the project SH-284-15. Michael Kliphuis (IMAU-UU) is thanked for his assistance in carrying out the numerical computations with the POP model. The authors thank two anonymous reviewers for their helpful comments. The analysis code is licensed under BSD-3-Clause and is archived at Zenodo as https://doi.org/10.5281/zenodo.1414359. Output from the ocean model simulation used in this work is available upon request to the corresponding author.

References

Behrens, E., Rickard, G., Morgenstern, O., Martin, T., Osprey, A., & Joshi, M. (2016). Southern Ocean deep convection in global climate models: A driver for variability of subpolar gyres and Drake Passage transport on decadal timescales. *Journal of Geophysical Research: Oceans*, *121*, 3905–3925. https://doi.org/10.1002/2015JC011286

Bischoff, T., & Thompson, A. F. (2014). Configuration of a Southern Ocean storm track. *Journal of Physical Oceanography*, *44*(12), 3072–3078. https://doi.org/10.1175/JPO-D-14-0062.1

Carsey, F. D. (1980). Microwave observation of the Weddell Polynya. *Monthly Weather Review*, *108*(12), 2032–2044. https://doi.org/10.1175/1520-0493(1980)108<2032:MOOTWP>2.0.CO;2

Chapman, C. C., Hogg, A. M., Kiss, A. E., & Rintoul, S. R. (2015). The dynamics of Southern Ocean storm tracks. *Journal of Physical Oceanography*, *45*(3), 884–903. https://doi.org/10.1175/JPO-D-14-0075.1

Delworth, T. L., & Zeng, F. (2012). Multicentennial variability of the Atlantic meridional overturning circulation and its climatic influence in a 4000 year simulation of the GFDL CM2.1 climate model. *Geophysical Research Letters*, *39*, L13702. https://doi.org/10.1029/2012GL052107

Dijkstra, H. A., & der Heydt, A. S. (2017). Basic mechanisms of centennial climate variability. *PAGES Magazine*, *25*(3), 150–151.

Dijkstra, H. A., Saenz, J. A., & McC Hogg, A. (2014). Energetics of multidecadal Atlantic Ocean variability. *Journal Of Climate*, *27*(20), 7874–7889.

Dufour, C. O., Morrison, A. K., Griffies, S. M., Frenger, I., Zanowski, H., & Winton, M. (2017). Preconditioning of the Weddell Sea polynya by the ocean mesoscale and dense water overflows. *Journal of Climate*, *30*(19), 7719–7737. https://doi.org/10.1175/JCLI-D-16-0586.1

Dukowicz, J. K., & Smith, R. D. (1994). Implicit free-surface method for the Bryan-Cox-Semtner ocean model. *Journal of Geophysical Research*, *99*(C4), 7991–8014. https://doi.org/10.1029/93JC03455

Ferrari, R., & Wunsch, C. (2009). Ocean circulation kinetic energy: Reservoirs, sources, and sinks. *Annual Review of Fluid Mechanics*, *41*(1), 253–282.

Gent, P. R. (2016). Effects of Southern Hemisphere wind changes on the meridional overturning circulation in ocean models. *Annual Review of Marine Science*, *8*(1), 79–94.

Gent, P. R., Large, W. G., & Bryan, F. O. (2001). What sets the mean transport through Drake Passage? *Journal of Geophysical Research*, *106*(C2), 2693–2712. https://doi.org/10.1029/2000JC900036

Gordon, A. L. (1978). Deep Antarctic convection west of Maud Rise. *Journal of Physical Oceanography*, *8*, 600–612.

Gordon, A. L. (1982). Weddell deep water variability. *Journal of Marine Science*, *40*, 199–217.

Griffies, S. M., Winton, M., Anderson, W. G., Benson, R., Delworth, T. L., Dufour, C. O., et al. (2015). Impacts on ocean heat from transient mesoscale eddies in a hierarchy of climate models. *Journal of Climate*, *28*(3), 952–977.

Heuzé, C., Heywood, K. J., Stevens, D. P., & Ridley, J. K. (2013). Southern Ocean bottom water characteristics in CMIP5 models. *Geophysical Research Letters*, *40*, 1409–1414. https://doi.org/10.1002/grl.50287

Hogg, A. M. C., & Blundell, J. R. (2006). Interdecadal variability of the Southern Ocean. *Journal of Physical Oceanography*, *36*(8), 1626–1645. https://doi.org/10.1175/JPO2934.1

Hogg, A. M., Spence, P., Saenko, O. A., & Downes, S. M. (2017). The energetics of Southern Ocean upwelling. *Journal of Physical Oceanography*, *47*(1), 135–153.

Howard, E., Hogg, A. M., Waterman, S., & Marshall, D. P. (2015). The injection of zonal momentum by buoyancy forcing in a Southern Ocean model. *Journal of Physical Oceanography*, *45*(1), 259–271.

Hurrell, J. W., Hack, J. J., Shea, D., Caron, J. M., & Rosinski, J. (2008). A new sea surface temperature and sea ice boundary dataset for the community atmosphere model. *Journal of Climate*, *21*(19), 5145–5153. https://doi.org/10.1175/2008JCLI2292.1

Jackson, L., & Vellinga, M. (2013). Multidecadal to centennial variability of the AMOC: HadCM3 and a perturbed physics ensemble. *Journal Of Climate*, *26*(7), 2390–2407.

Kjellsson, J., Holland, P. R., Marshall, G. J., Mathiot, P., Aksenov, Y., Coward, A. C., et al. (2015). Model sensitivity of the Weddell and Ross seas, Antarctica, to vertical mixing and freshwater forcing. *Ocean Modelling*, *94*, 141–152. https://doi.org/10.1016/j.ocemod.2015.08.003

Large, W. G., & Yeager, S. G. (2004). Diurnal to decadal global forcing for ocean and sea-ice models: the data sets and flux climatologies (*Tech. Rep. May*). Boulder, Colorado: NCAR. https://doi.org/10.5065/D6KK98Q6

Latif, M., Martin, T., & Park, W. (2013). Southern Ocean sector centennial climate variability and recent decadal trends. *Journal Of Climate*, *26*(19), 7767–7782.

Latif, M., Martin, T., Reintges, A., & Park, W. (2017). Southern Ocean decadal variability and predictability. *Current Climate Change Reports*, *3*, 163–173.

Le Bars, D., Viebahn, J. P., & Dijkstra, H. A. (2016). A Southern Ocean mode of multidecadal variability. *Geophysical Research Letters*, *43*, 2102–2110. https://doi.org/10.1002/2016GL068177

Lorenz, E. (1955). Available potential energy and the maintenance of the general circulation. *Tellus*, *7*, 157–167.

Maltrud, M., Bryan, F., & Peacock, S. (2010). Boundary impulse response functions in a century-long eddying global ocean simulation. *Environmental Fluid Mechanics*, *10*(1-2), 275–295. https://doi.org/10.1007/s10652-009-9154-3

Martin, T., Park, W., & Latif, M. (2013). Multi-centennial variability controlled by Southern Ocean convection in the Kiel Climate Model. *Climate Dynamics*, *40*(7), 2005–2022. https://doi.org/10.1007/s00382-012-1586-7

Mayewski, P. A., Meredith, M. P., Summerhayes, C. P., Turner, J., Worby, A., Barrett, P. J., et al. (2009). State of the Antarctic and Southern Ocean climate system. *Reviews of Geophysics*, *47*, RG1003. https://doi.org/10.1029/2007RG000231

Oort, A. H., & Peixóto, J. P. (1983). Global angular momentum and energy balance requirements from observations. In B. Saltzman (Ed.), *Theory of Climate, Advances in Geophysics* (Vol. 25, pp. 355–490). New York, USA: Elsevier. https://doi.org/10.1016/S0065-2687(08)60177-6

Park, W., & Latif, M. (2008). Multidecadal and multicentennial variability of the meridional overturning circulation. *Geophysical Research Letters*, *35*, L22703. https://doi.org/10.1029/2008GL035779

Scambos, T., Stammerjohn, S., & Eds (2018). Antarctica [in "State of the Climate in 2017"]. *Bulletin of the American Meteorological Society*, *99*(August), 175–192. https://doi.org/10.1175/2018BAMSStateoftheClimate.1

Smith, R., Jones, P., Briegleb, B., Bryan, F., Danabasoglu, G., Dennis, J., et al. (2010). The parallel ocean program (POP) reference manual (Tech. Rep.). Los Alamos, New Mexico, USA: Los Alamos National Laboratory (LANL).

Spall, M. A., & Pickart, R. S. (2001). Where does dense water sink? A subpolar gyre example. *Journal of Physical Oceanography*, *31*, 810–826.

Stössel, A., Notz, D., Haumann, F. A., Haak, H., Jungclaus, J., & Mikolajewicz, U. (2015). Controlling high-latitude Southern Ocean convection in climate models. *Ocean Modelling*, *86*, 58–75. https://doi.org/10.1016/j.ocemod.2014.11.008

Su, Z., Ingersoll, A. P., Stewart, A. L., & Thompson, A. F. (2016a). Ocean convective available potential energy. Part I: Concept and calculation. *Journal of Physical Oceanography*, *46*, 1081–1096.

Su, Z., Ingersoll, A. P., Stewart, A. L., & Thompson, A. F. (2016b). On the minimum potential energy state and the eddy size constrained APE density. *Journal of Physical Oceanography*, *46*, 2663–2674.

Thompson, A. F., & Naveira Garabato, A. C. (2014). Equilibration of the Antarctic circumpolar current by standing meanders. *Journal of Physical Oceanography*, *44*(7), 1811–1828. https://doi.org/10.1175/JPO-D-13-0163.1

van Westen, R. M., & Dijkstra, H. A. (2017). Southern Ocean origin of multidecadal variability in the North Brazil current. *Geophysical Research Letters*, *44*, 10,510–540,548. https://doi.org/10.1002/2017GL074815

von Storch, J.-S., Eden, C., Fast, I., Haak, H., Hernández-Deckers, D., Maier-Reimer, E., et al. (2012). An estimate of the Lorenz energy cycle for the World Ocean based on the STORM/NCEP simulation. *Journal of Physical Oceanography*, *42*(12), 2185–2205. https://doi.org/10.1175/JPO-D-12-079.1

Weijer, W., Maltrud, M. E., Hecht, M. W., Dijkstra, H. A., & Kliphuis, M. A. (2012). Response of the Atlantic Ocean circulation to Greenland Ice Sheet melting in a strongly-eddying ocean model. *Geophysical Research Letters*, *39*, L09606. https://doi.org/10.1029/2012GL051611

Winton, M. (1995). Energetics of deep-decoupling oscillations. *Journal of Physical Oceanography*, *25*(3), 420–427.

Wu, Y., Wang, Z., & Liu, C. (2017). On the response of the Lorenz energy cycle for the Southern Ocean to intensified westerlies. *Journal of Geophysical Research: Oceans*, *122*, 2465–2493. https://doi.org/10.1002/2016JC012539